# An $H_\infty$ Observer-based 3-D Thermal Monitoring Method for Multi-chip IGBT Modules with Robustness to Model Parameter and Power Loss Uncertainty

Ye Tian, *Student Member*, *IEEE*, Bowen Liu, *Student Member*, *IEEE*, Chushan Li, *Member*, *IEEE*, Bowei Chen, Bin Guo, Yongjun Zheng, Haoze Luo, *Senior Member*, *IEEE*, Wuhua Li, *Senior Member*, *IEEE*, and Xiangning He, *Fellow*, *IEEE*

***Abstract*—Dynamic temperature monitoring at critical locations of IGBT modules is a key means to improve the reliability of high-power converters. However, most existing thermal model-based methods suffer from temperature estimation errors due to model parameter variations and loss calculation errors. To address this problem, based on the reduced-order thermal model, an $H_\infty$ observer-based robust 3-D thermal monitoring method for IGBT modules is proposed in this paper. Through the optimized design of the observer feedback gain, the thermal model and real-time temperature information are effectively combined, which reduces the temperature estimation error in the worst case. Thus, the proposed method is more robust to model parameter uncertainty and loss error than the conventional temperature observers. Experiment validations of the proposed $H_\infty$ observer and conventional observers are provided. The results demonstrate that the proposed observer achieves the highest temperature estimation accuracy under various system uncertainties, making it an effective solution for reliable online thermal monitoring of IGBT modules over the whole life cycle.**

***Index Terms*—IGBT module, uncertainty, robustness, junction temperature, thermal monitoring, reliability.**

Received: May 29, 2024
Accepted: September 13, 2024
Published Online: May 1, 2025

Ye Tian, Bowen Liu, Bowei Chen, Haoze Luo, Wuhua Li, and Xiangning He are with the College of Electrical Engineering, Zhejiang University, Hangzhou 310027, China (e-mail: tianbobing@outlook.com; 22210083@zju.edu.cn; cbw1030@163.com; haozeluo@zju.edu.cn; woohualee@zju.edu.cn; hxn@ zju.edu.cn).

Chushan Li (corresponding author) is with the Zhejiang University-University of Illinois at Urbana-Champaign Institute, Zhejiang University, Hangzhou 310027, China (e-mail: chushan@intl.zju.edu.cn).

Bin Guo is with Hangzhou Wolei Intelligent Technology Co., Ltd., Hangzhou 310018, China (e-mail: guobin@wolei-tech.com).

Yongjun Zheng is with the College of Metrology and Measurement Engineering, China Jiliang University, Hangzhou 310018, China (e-mail: davidzhyj@cjlu.edu.cn).

DOI: 10.23919/PCMP.2024.000141

## I. Introduction

High-power converters, as critical power conversion equipment, are widely used in wind power, photovoltaic generation, energy storage, and HVDC applications [1], [2]. Multi-chip IGBT modules with high power density are the core components of high-power converters. However, recent studies have shown that IGBT modules are the most vulnerable components in high-power converters, with the main failure factors being over-temperature damage and aging caused by thermal-mechanical stresses. Temperature monitoring for IGBT is the prerequisite for over-temperature protection, online lifetime prediction, and active thermal management, and is the key to improving the reliability of high-power converters.

Nowadays, many methods are available to yield the temperature inside the IGBT modules, such as infrared thermography, fiber optics, physical sensors, and thermosensitive electrical parameters (TSEPs) [3], [4]. However, the applications of these methods are hindered by several challenges, such as high cost, damage to module packaging, low sensitivity, susceptibility to electromagnetic interference (EMI), coupling with operating conditions, and limited spatial resolution. In contrast, the thermal model method has the advantages of non-invasiveness, insensitivity to EMI noise, and the ability to estimate the temperatures at specific spatial locations [5]–[21]. Among them, the thermal network models balance accuracy and model complexity, thus making them suitable for long-term thermal analysis and online temperature monitoring for IGBT modules.

The 1-D Foster thermal network and the 1-D Cauer thermal network are two typical thermal network models. The parameters of the 1-D Foster model can be obtained by fitting the transient thermal impedance curve, but the parameters do not reflect the physical properties of the

IGBT. In contrast, the 1-D Cauer model is constructed based on the packaging structure and material properties, so the parameters in this type of model have physical meanings.

However, applying 1-D thermal network models to multi-chip IGBT modules may underestimate the junction temperature due to neglecting the thermal cross-coupling (TCC) effect. To tackle this challenge, a 3-D Foster model is developed in [10], in which the self-heating and cross-coupling thermal impedances are combined by the superposition theorem to account for TCC effect. 3-D Cauer models with physical meaning were proposed in [11] and [12], which are also suitable for monitoring temperatures at specific locations in multichip IGBT modules. A novel two-step parameter extraction method [13] and level-based learning swarm optimization (LLSO) method [14] are employed to further improve the efficiency of the identification of parameters in the 3-D Cauer model. Reference [15] considers the temperature dependence of material thermal parameters and improved the model in [13], enhancing the accuracy of the 3-D Cauer model within the full temperature range. However, the parameter identification of the thermal models in [10]–[15] relies on finite element method (FEM) transient simulation, which is time-consuming. In [16]–[19], by only utilizing the thermal flux curves obtained from steady-state FEM simulation, the parameters of a 3-D temperature-dependent thermal model were analytically calculated. To reduce the complexity of the thermal network model, a decoupled thermal model decomposing the 3-D thermal network into 1-D analytical Cauer models [20] and an average 2-D thermal model [21] are proposed.

Accurate power loss information and thermal model parameters are necessary for precisely estimating junction temperature in the thermal model method. However, as shown in Fig. 1, in the whole life cycle of IGBT modules, due to manufacturing tolerances, boundary condition variation, and calibration error, the calculated power loss and parameters of the thermal model have deviations $\Delta P$, $\Delta R$, and $\Delta C$ from the actual values in the initial stage. These deviations will further increase due to the aging of the solder layer, thermal interface material (TIM), cooling system, and bonding wire [22]–[29]. However, most existing thermal model methods do not adequately address the impact of these uncertainties, leading to significant temperature estimation errors $\Delta T$.

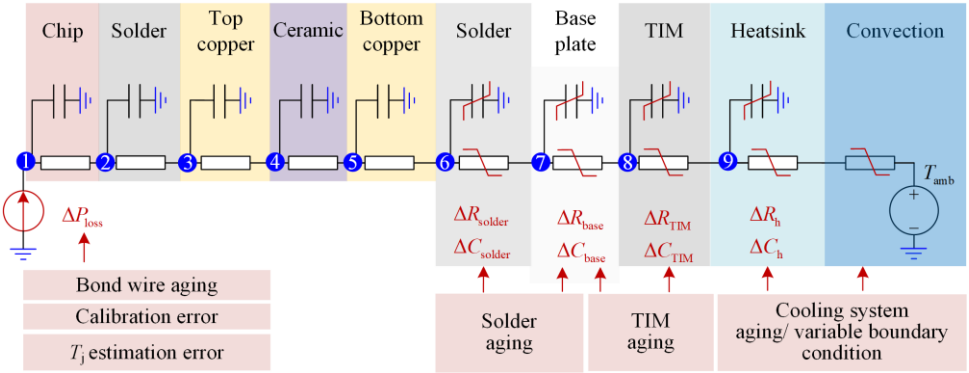


Fig. 1. Thermal model parameter and power loss errors of IGBT.

Several technologies have been proposed to mitigate the impact of parameter variation caused by one specific mechanism. For instance, a recursive least squares approach is proposed to rectify thermal model parameter deviation due to cracks in solder [23]. Furthermore, the relationship between lateral temperature gradients on the case and crack length of direct bond copper (DBC) solder is established in [24], [25]. For cooling system degradation, an online identification method is introduced for air duct blockage degree [27], followed by analytical calculation of heatsink thermal parameters [28]. Additionally, methods in [30] and [31] improve the accuracy of the thermal model under variable boundary conditions by fitting model parameters as functions of flow rate and selecting negative temperature coefficient (NTC) as temperature reference point, respectively.

However, in practice, multiple aging mechanisms coexist, causing thermal parameter deviations in the solder layer, TIM layer, and heat sink simultaneously. The cooling temperature-curve-based method [32] and dual Kalman filter (DKF) based method [33] are proposed to identify all thermal resistances and capacitances in the thermal model, with the potential to mitigate the adverse effects of thermal model parameter errors caused by multiple aging mechanisms on temperature estimation. However, accurate loss information or junction temperature, which is challenging to obtain in real time, is required in these methods. To further improve the accuracy of loss calculation, a conduction loss online correction method based on the Levenberg-Marquardt algorithm is proposed for press-pack IGBTs [34], but it is not robust enough to model parameter variations. Reference [35] estimates power loss using lead temperature measurements, but this method compromises insulation performance and limits its applicability in medium and high-voltage applications. In summary, the performance of the above methods will be degraded in the simultaneous presence of both model parameter and power loss uncertainties.

Compared with open-loop thermal models, temperature observers potentially offer a more robust solution by combining the measurement information and the model. For instance, a proportional-integral (PI)-based observer is used to identify the thermal resistances and capacitances of the solder layer [36], while references [5] and [37] propose temperature observers based on PI and adaptive artificial neural network (ANN), respectively, to compensate for power loss error. However, these methods necessitate junction temperature information, which is challenging to acquire online. A Luenberger observer is proposed offering robustness to variable boundary conditions [38], whereas an unknown input observer [39] based on NTC temperature is utilized to simultaneously estimate junction temperature and power loss. Additionally, Kalman filters can achieve optimal temperature estimation under zero-mean Gaussian noise [40], [41]. However, due to the model parameter and power loss uncertainties with unknown statistical characteristics, temperature estimation accuracy cannot be guaranteed theoretically by observers in [5], [36]–[41]. Although an NTC-based adaptive observer can correct power loss and model parameters without prior knowledge of the uncertainties [42], it only applies to single-chip IGBT modules. The comparative analysis of the above existing methods is shown in Table I (The ☆ represents approximately 1/2 performance of the ★).

TABLE I
COMPARISON OF EXISTING METHODS AND PROPOSED METHOD

| Method | Robustness | | | | | Universal | Online |
|---|---|---|---|---|---|---|---|
| | Solder aging | TIM aging | Cooling system aging | Variable boundary condition | Power loss error | | |
| [23] | ★★★ | × | × | × | × | ★★★ | √ |
| [22], [24], [25], [26] | ★★★ | × | × | × | × | ★★ | √ |
| [27], [28] | × | × | ★★★ | ★★★ | × | ★★★ | √ |
| [30] | × | × | × | ★★★ | × | ★★★ | √ |
| [31] | × | × | ★★ | ★★★ | × | ★★★ | √ |
| [32] | ★★★ | ★★★ | ★★★ | ★★★ | × | ★ | × |
| [33] | ★★★ | ★★★ | ★★★ | ★★★ | × | ★★★ | √ |
| [34] | × | × | × | × | ★★ | ★ | √ |
| [35] | ☆ | ☆ | ☆ | ☆ | ★★★ | ☆ | √ |
| [36] | ★★★ | × | × | × | × | ★★ | √ |
| [5], [37] | ★ | ★ | ★ | ★ | ★★★ | ★ | √ |
| [38] | ☆ | ☆ | ★★☆ | ★★☆ | ☆ | ★★★ | √ |
| [39] | × | × | × | × | ★★★ | ☆ | √ |
| [40], [41] | ☆ | ☆ | ☆ | ☆ | ☆ | ★★★ | √ |
| [42] | ★☆ | ★☆ | ★☆ | ★☆ | ★★★ | ☆ | √ |
| Proposed observer | ★★☆ | ★★☆ | ★★☆ | ★★☆ | ★★☆ | ★★★ | √ |

As shown in Table I, the main limitation of the existing methods is that most of them are only robust to parameter errors caused by one specific aging mechanism or to power loss calculation errors. However, in real-world scenarios, solder, TIM, and cooling systems may age simultaneously, along with power loss calculation errors, leading to unsatisfactory junction temperature estimation accuracy.

To enhance the reliability of thermal monitoring of IGBT modules in the whole life cycle, a 3-D robust temperature estimation method is proposed, in which the $H_\infty$ observer is combined with a reduced order thermal model (ROM) of IGBT for the first time, as shown in Fig. 2. The proposed technology effectively fuses the thermal model with the measurement information, resulting in satisfactory 3-D real-time temperature estimations even with power loss and thermal model parameter errors.

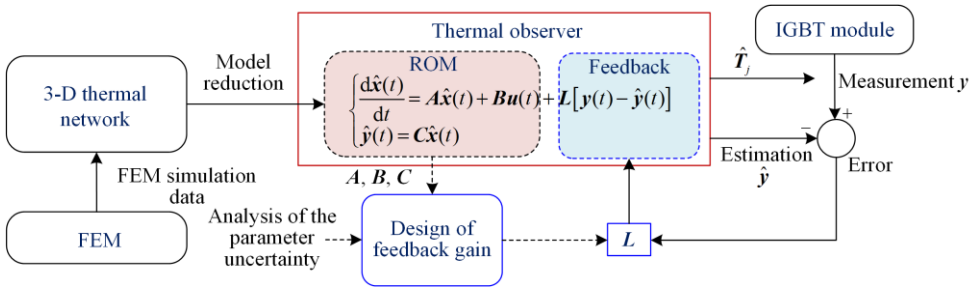


Fig. 2. The principle of the proposed 3-D robust online temperature monitoring method.

The rest of the paper is organized as follows. In Section II, based on FEM and model reduction technique, a 3-D thermal reduced order model (3-D thermal ROM) is proposed. In Section III, based on the ROM, the observer gain is optimized to improve its robustness and reliability by reducing the estimation error in the worst case under all possible cases of parameter uncertainties. Section IV provides comparative experiment validations of the proposed $H_\infty$ observer, traditional Luenberger observer, Kalman filter, and open loop thermal model. Finally, Section V concludes the paper.

## II. Thermal Model of IGBT Module

The critical component of the 3-D $H_\infty$ temperature observer is the reduced-order 3-D thermal ROM. The 3-D thermal ROM is derived via model reduction of a 3-D lumped parameter thermal network model, whose parameters are identified based on FEM simulations. In the following section, the modeling method for the FEM model and the 3-D thermal network of the IGBT module, and the model reduction technology are discussed.

### A. FEM Modeling of the IGBT Module in Ansys Icepak

The 1700 V/450 A EconoDUAL half bridge IGBT module 2MBI450VN-170 is investigated in this paper, which consists of three paralleled IGBT chips and diode chips within each bridge arm. Its internal structure, circuit topology, and cross-sectional package diagramare illustrated in Fig. 3. The lower arm IGBT chips, lower arm diode chips, upper arm IGBT chips, and upper arm diode chips are named as $T_{LBi}$, $D_{LBi}$, $T_{HBi}$, and $D_{HBi}$ $(i=1,2,3)$, respectively. A forced air-cooling heatsink with TIM is installed under the IGBT module.

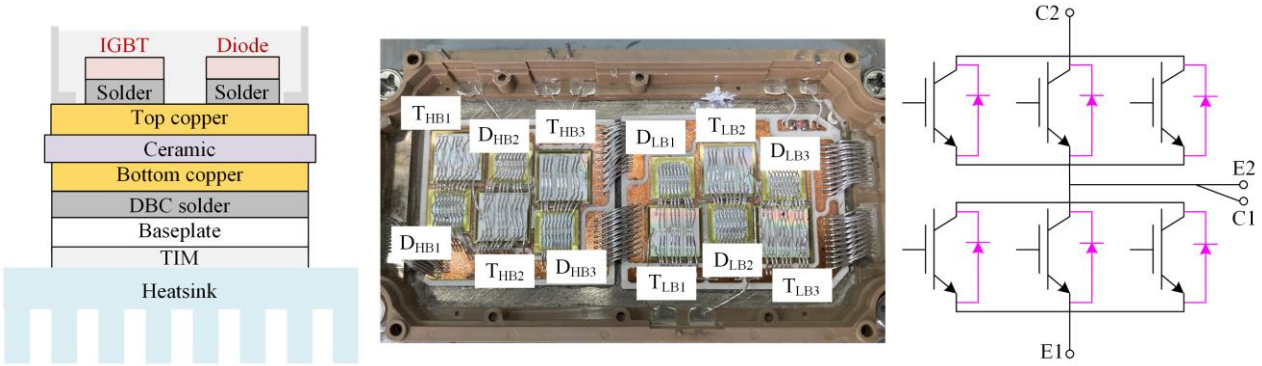


Fig. 3. Structure of the IGBT module.

As shown in Fig. 4, Sensor1 and Sensor2 are positioned at the bottom of the case, while Sensor3 is located on the upper surface of the ceramic, which can provide feedback to the temperature observer for real-time correction of the thermal model. Ansys Icepak is used to solve the temperature and fluid fields within the IGBT module and heatsink.

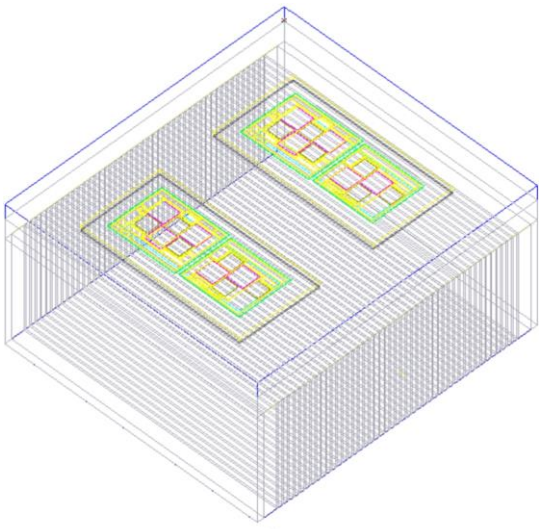

(a)

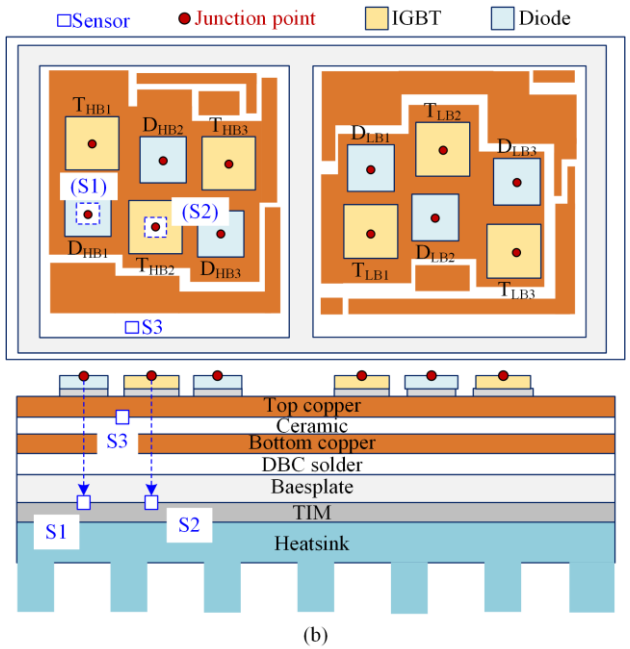


(b)

Fig. 4. FEM model of the IGBT module and sensor locations. (a) Icepak FEM model of the IGBT module. (b) Sensor locations.

As illustrated in Fig. 4, the dominant heat transfer mechanism is heat conduction from the chip to the

heatsink, followed by thermal convection. Thus, bonding wires, internal silicone gel, and radiation are neglected to simplify the FEM model. The enhanced realizable two-equation turbulence model is employed for the fluid region. Material properties for the FEM model are detailed in Table II.

TABLE II
MATERIAL PARAMETERS OF ICEPAK FEM MODEL OF THE IGBT MODULE AND HEATSINK

| Material | Height (mm) | Conductivity (W/(m·K)) | Density (kg/m$^3$) | Specific heat capacity (J/(kg·K)) |
|---|---|---|---|---|
| Chip | 0.195 | 130 | 2330 | 702 |
| Chip solder | 0.100 | 46 | 9000 | 288 |
| Top copper | 0.375 | 400 | 8700 | 385 |
| Ceramic | 0.323 | 30 | 1700 | 880 |
| Bottom copper | 0.377 | 154 | 2700 | 896 |
| DBC solder | 0.279 | 46 | 900 | 288 |
| Baseplate | 3.000 | 400 | 8700 | 385 |
| TIM | 1.000 | 8 | 3500 | 907 |
| Heatsink top plate | 15.000 | 237 | 2700 | 880 |

### *B. 3-D Thermal Network Model of the IGBT Module*

The FEM model in Fig. 4 is computationally expensive and unsuitable for real-time temperature estimation. To address this, a 3-D Cauer/Foster hybrid thermal network model, as illustrated in Fig. 5, is proposed, which balances model accuracy and computational efficiency.

Compared to the existing thermal models [10]–[21], the proposed model shows advantages in both accuracy and observability, while observability is a necessary condition for temperature observer design. The temperatures of nodes 1, 2, ⋯, 162 in the IGBT module and heatsink can be estimated by the 3-D thermal network model. The lines between nodes in Fig. 5 represent thermal resistances. The hybrid model in Fig. 5 consists of 3-D Cauer and Foster networks. To ensure the observability of the model, the 3-D Cauer network is used to model the region above the bottom of the heatsink plate, enabling the estimation of temperatures within the IGBT module, TIM, and heatsink plate. The local details of the 3-D Cauer model are illustrated in the red dashed box in the upper left corner of Fig. 5. $T_i$ and $C_i$ represent the temperature and thermal capacitance of node *i*, respectively. $R_{i\_j}$ represents the thermal resistance between node *i* and node *j*. The losses of $\mathrm{T}_{\mathrm{LB}i}$, $\mathrm{D}_{\mathrm{LB}i}$, $\mathrm{T}_{\mathrm{HB}i}$, and $\mathrm{D}_{\mathrm{HB}i}$ $(i=1,2,3)$ are represented as $P_{\mathrm{TLB}}$, $P_{\mathrm{DLB}}$, $P_{\mathrm{THB}}$, and $P_{\mathrm{DHB}}$, respectively. All nodes are located on the upper surface of the corresponding layer. Nodes 1, 2, ⋯, and 12 are positioned at the center of the chip surface. Nodes 39, 42, 45, 48, 51, and 54 are candidate locations for temperature sensors on the upper surface of the ceramic layer. Nodes 145, 146, 147,⋯, 162 at the bottom of the heatsink plate are the temperature reference nodes for the 3-D Cauer model. The temperatures of these reference nodes serve as the boundary conditions for the 3-D Cauer model. Taking node 147 as an example, its temperature can be estimated using an 8th order Foster thermal network, which is mathematically equivalent to the convection process, as shown in the red dashed box in the lower left corner of Fig. 5. $T_{h147\_1}$, $T_{h147\_2},\cdots,T_{h147\_8}$ represent the temperatures of the thermal capacitances in the Foster model. $R_{h147\_i}$ and $C_{h147\_i}(i=1,2,\cdots,8)$ represent the thermal resistances and capacitances of the Foster model. $Z_{th147\_\mathrm{TLB}}$, $Z_{th147\_\mathrm{DLB}}$, $Z_{th147\_\mathrm{THB}}$, and $Z_{th147\_\mathrm{DHB}}$ are the transient thermal impedances of the Foster model. $T_{\mathrm{amb}}$ is the ambient temperature.

The thermal resistances and capacitances in the 3-D Cauer model are identified based on FEM steady-state and transient simulations using the non-negative least squares method and pattern search method, respectively. The parameters in the Foster model are identified using the nonlinear least squares method by fitting the transient thermal impedance obtained from FEM transient simulation. Detailed parameter identification and loss modeling methods can be found in [10] and [30]. A Matlab program is developed for automatic parameter identification.

The state space of the 3-D hybrid thermal network model in Fig. 5 can be expressed by:

$$G:\begin{cases}\dfrac{\mathrm{d}\boldsymbol{T}}{\mathrm{d}t}=\boldsymbol{A}_{\mathrm{h}}\boldsymbol{T}+\boldsymbol{B}_{\mathrm{h}}\boldsymbol{u}\\ \boldsymbol{T}_{\mathrm{sensor}}(t)=\boldsymbol{C}_{\mathrm{h}}\boldsymbol{T}\\ \boldsymbol{T}_{\mathrm{out}}(t)=\boldsymbol{H}_{\mathrm{h}}\boldsymbol{T}\end{cases}\tag{1}$$

where $\boldsymbol{T}$ is the vector of states; $\boldsymbol{T}_{\mathrm{sensor}}$ is the vector of temperature measurements from Sensor1 to Sensor3 (node 42, node 110, node 113); $\boldsymbol{T}_{\mathrm{out}}$ can consist of any nodes within the thermal network based on specific applications, and in this paper, the temperature of the IGBT chip (node 2), Diode chip (node 4), and DBC solder (node 74 and node 77) are selected to form $\boldsymbol{T}_{\mathrm{out}}$ as an example; the elements in the coefficient matrices $\boldsymbol{A}_{\mathrm{h}}$, $\boldsymbol{B}_{\mathrm{h}}$, $\boldsymbol{C}_{\mathrm{h}}$, and $\boldsymbol{H}_{\mathrm{h}}$ of the state space *G* can be calculated according to [43]; while the observability of system *G* can be determined by the rank criterion [46]; and there are:

$$\boldsymbol{T}=[T_1\quad T_2\quad\cdots\quad T_{144}\quad\cdots\quad T_{h162\_8}]^{\mathrm{T}}\tag{2}$$

$$\boldsymbol{u}=[P_{\mathrm{TLB}}\quad P_{D\mathrm{LB}}\quad P_{\mathrm{THB}}\quad P_{\mathrm{DHB}}\quad T_{\mathrm{amb}}]^{\mathrm{T}}\tag{3}$$

$$\boldsymbol{T}_{\mathrm{sensor}}=[T_{42}\quad T_{110}\quad T_{113}]^{\mathrm{T}}\tag{4}$$

$$\boldsymbol{T}_{\mathrm{out}}=[T_2\quad T_4\quad T_{74}\quad T_{77}]^{\mathrm{T}}\tag{5}$$

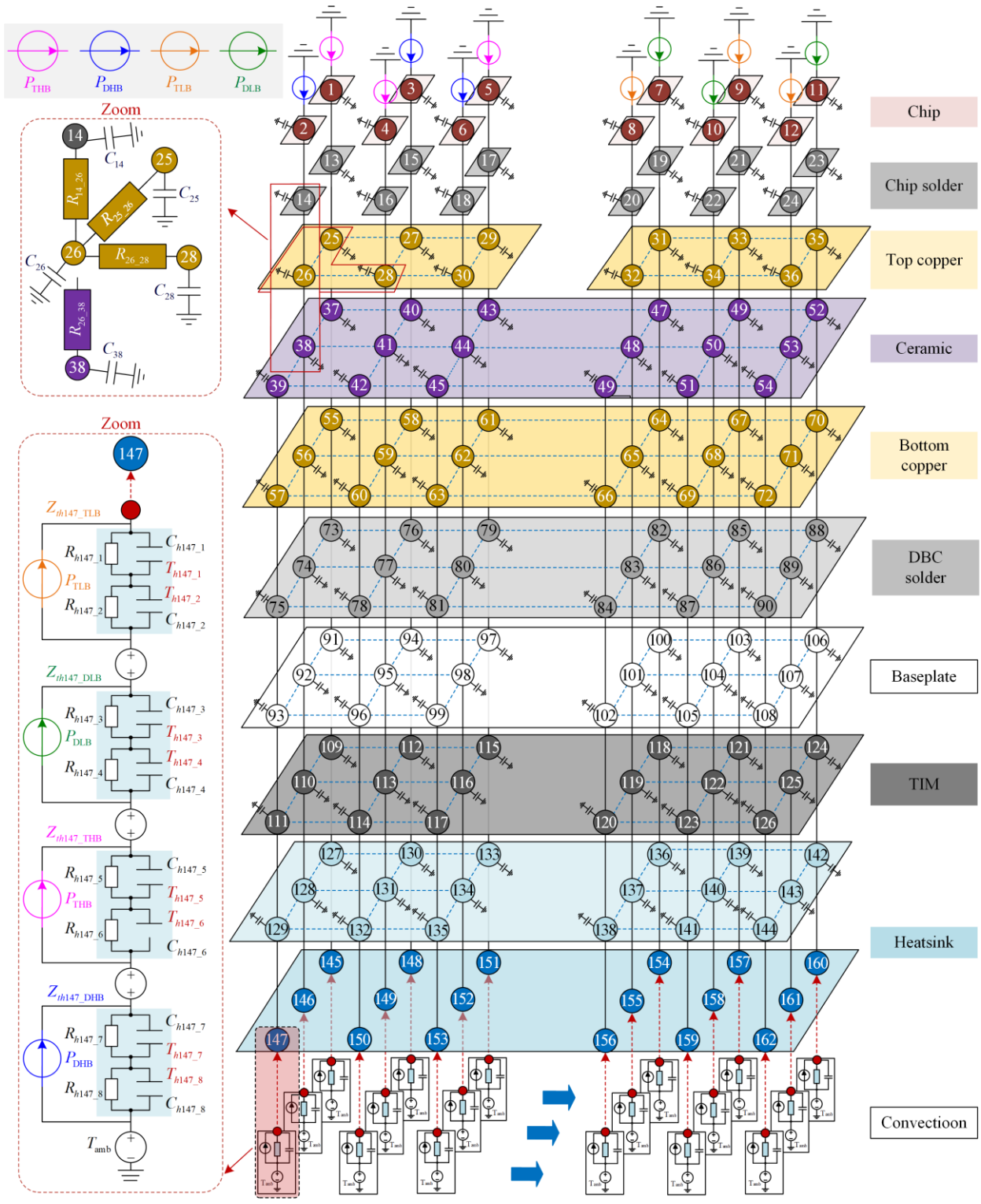


Fig. 5. 3-D Cauer/Foster hybrid thermal network model of the IGBT module and heat sink.

Figure 6(a) compares the transient junction temperature responses predicted by the thermal network and the FEM (when $T_{amb}=10\,°C$, $P_{TLB}=50\,W$, $P_{DLB}=60\,W$, $P_{THB}=70\,W$, and $P_{DHB}=80\,W$), while Fig. 6(b) illustrates the temperature distribution within the IGBT module obtained from ICEPAK at 150 s under the same operating condition. As evidenced from Fig. 6, the proposed thermal network achieves excellent agreement with the FEM, exhibiting a maximum error of less than 3%.

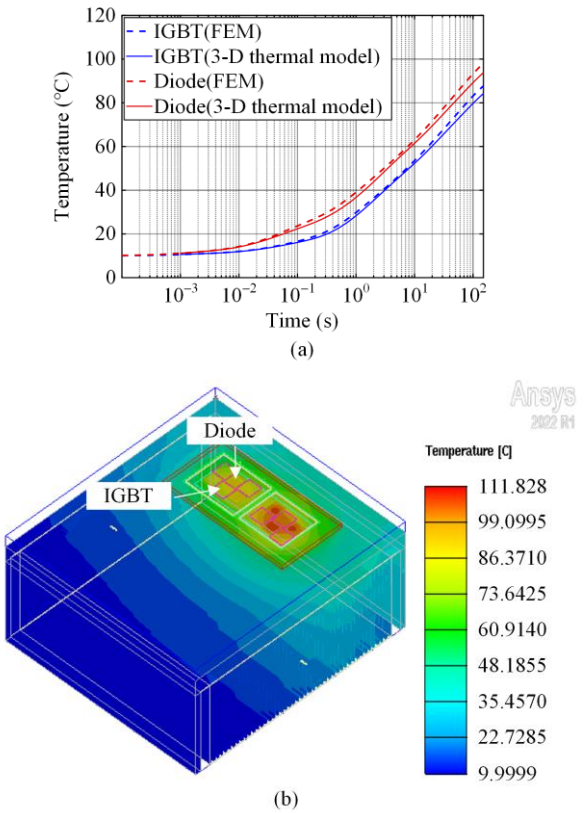


Fig. 6. Comparison between the 3-D thermal network and the FEM model. (a) Transient temperature comparison between the 3-D hybrid thermal network and FEM model. (b) Temperature distribution of the IGBT module in ICEPAK at $t$ =150 s.

### *C. Thermal Model Reduction*

While the thermal network model in Fig. 5 offers a significant model reduction compared to the FEM model in Icepak, its state space still has a high order of 288th. This presents challenges for real-time applications and observer gain design. Therefore, the model reduction technique based on the balanced truncation method is applied to reduce the order of the original high-order thermal model in (1) with a potentially small loss of model accuracy [44].

Based on the transformation matrix [44], the original model ($G$) can be transformed into the system $G_{\mathrm{M}}$ as:

$$G_{\mathrm{M}}:\begin{cases}\dfrac{\mathrm{d}}{\mathrm{d}t}\begin{bmatrix}\boldsymbol{x}\\ \boldsymbol{\eta}\end{bmatrix}=\begin{bmatrix}\boldsymbol{A} & \boldsymbol{A}_{x\eta}\\ \boldsymbol{A}_{\eta x} & \boldsymbol{A}_{\eta\eta}\end{bmatrix}\begin{bmatrix}\boldsymbol{x}\\ \boldsymbol{\eta}\end{bmatrix}+\begin{bmatrix}\boldsymbol{B}\\ \boldsymbol{B}_{\eta}\end{bmatrix}\boldsymbol{u}\\ \boldsymbol{T}_{\mathrm{sensor}}(t)=\begin{bmatrix}\boldsymbol{C} & \boldsymbol{C}_{\eta}\end{bmatrix}\begin{bmatrix}\boldsymbol{x}\\ \boldsymbol{\eta}\end{bmatrix}\\ \boldsymbol{T}_{\mathrm{out}}(t)=\begin{bmatrix}\boldsymbol{H} & \boldsymbol{H}_{\eta}\end{bmatrix}\begin{bmatrix}\boldsymbol{x}\\ \boldsymbol{\eta}\end{bmatrix}\end{cases} \tag{6}$$

where $\boldsymbol{x}$ and $\boldsymbol{\eta}$ are the states to be retained and truncated, respectively; $\boldsymbol{A}$, $\boldsymbol{A}_{x\eta}$, $\boldsymbol{A}_{\eta x}$, $\boldsymbol{A}_{\eta\eta}$, $\boldsymbol{B}$, $\boldsymbol{B}_{\eta}$, $\boldsymbol{C}$, and $\boldsymbol{C}_{\eta}$ are the coefficient matrices of $G_{\mathrm{M}}$.

The state variables in $G_{\mathrm{M}}$ are arranged in descending order according to their contributions to the energy transfer from $\boldsymbol{u}$ to $\boldsymbol{T}_{\mathrm{sensor}}$ and $\boldsymbol{T}_{\mathrm{out}}$. By truncating states $\boldsymbol{\eta}$ that have negligible contributions to the energy transfer, the original model ($G$) is reduced to a reduced-order model ($G_{\mathrm{BT}}$), as shown in (7), while retaining the dominant input-output behavior of $G$. In (7), $\boldsymbol{y}$ and $\boldsymbol{z}$ represent the approximations of $\boldsymbol{T}_{\mathrm{sensor}}$ and $\boldsymbol{T}_{\mathrm{out}}$, respectively.

$$G_{\mathrm{BT}}:\begin{cases}\dfrac{\mathrm{d}\boldsymbol{x}}{\mathrm{d}t}=\boldsymbol{A}\boldsymbol{x}+\boldsymbol{B}\boldsymbol{u}\\ \boldsymbol{y}(t)=\boldsymbol{C}\boldsymbol{x}\\ \boldsymbol{z}(t)=\boldsymbol{H}\boldsymbol{x}\end{cases} \tag{7}$$

The model reduction brings a truncation error between ROM ($G_{\mathrm{BT}}$) and $G$, which is negatively correlated with the order of $G_{\mathrm{BT}}$. The relative truncation error (RTE) is chosen as the metric to evaluate the accuracy of the ROM [44]. The relationship between the order of $G_{\mathrm{BT}}$ and the RTE is shown in Fig. 7. As seen, when the order of $G_{\mathrm{BT}}$ is less than 17th, the RTE increases sharply. Therefore, to strike a balance between model complexity and accuracy, the order of $G_{\mathrm{BT}}$ is determined to be 17th.

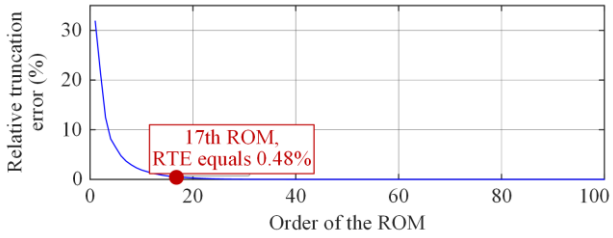


Fig. 7. Relative truncation error with different order of the ROM.

Let $T_{\mathrm{j}}$ and $T_{\mathrm{j\_BT}}$ denote the temperatures of the IGBT chip ($T_{\mathrm{HB2}}$) estimated by $G$ and $G_{\mathrm{BT}}$, respectively. To more intuitively demonstrate the error between $G$ and $G_{\mathrm{BT}}$, $|T_{\mathrm{j\_BT}}(\mathrm{j}\omega)/T_{\mathrm{j}}(\mathrm{j}\omega)|$ in the frequency domain and $T_{\mathrm{j\_BT}}(t)$ in the time domain with different ROM orders are illustrated in Fig. 8 and Fig. 9, respectively. For the 17th order ROM, the $|T_{\mathrm{j\_BT}}(\mathrm{j}\omega)/T_{\mathrm{j}}(\mathrm{j}\omega)|$ within [0, 100 Hz] is less than 0.72%, and the relative error between the maximum values of $T_{\mathrm{j\_BT}}(t)$ and $T_{\mathrm{j}}(t)$ is 0.10%, which shows that the 17th order $G_{\mathrm{BT}}$ achieves acceptable accuracy and can be the model foundation for the observer.

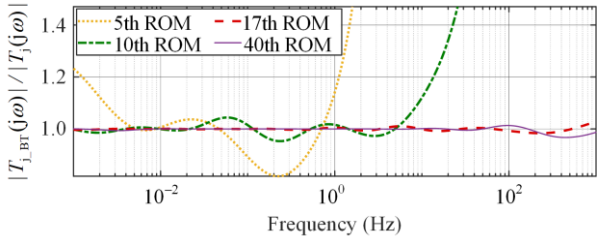


Fig. 8. $|T_{\mathrm{j\_BT}}(\mathrm{j}\omega)/T_{\mathrm{j}}(\mathrm{j}\omega)|$ with different orders of the ROM.

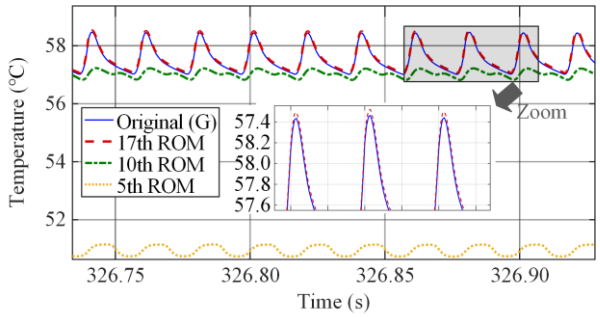


Fig. 9. $T_{\text{j\_BT}}(t)$ estimated by ROMs with different orders (half bridge, 50 Hz, 144 A, modulation ratio equals 0.9).

## III. $H_\infty$ Robust Thermal Observer

As highlighted in Section I, uncertainties in both power loss and model parameters introduce significant errors in the temperature estimation of the open-loop thermal model. To address this challenge, based on the ROM developed in Section II, a 3-D $H_\infty$ temperature observer is proposed, which can effectively combine the thermal model and real-time measurements to compensate for modeling errors. A vital advantage of the proposed observer is its robustness to system uncertainties, which surpasses conventional temperature observers such as the Luenberger observer designed based on pole placement and the Kalman filter. In this section, the root causes of temperature estimation error of the proposed observer are analyzed. Subsequently, the optimal design methodology for the observer feedback gain $\boldsymbol{L}$ under uncertainties is derived.

### *A. Root Cause Analysis of the Estimation Error of the Observer*

Based on the ROM ($G_{\text{BT}}$), an $H_\infty$ observer in (8) is proposed, as shown in Fig. 10.

$$\begin{cases} \dfrac{\mathrm{d}\hat{\boldsymbol{x}}(t)}{\mathrm{d}t} = \boldsymbol{A}\hat{\boldsymbol{x}}(t) + \boldsymbol{B}\boldsymbol{u}(t) + \boldsymbol{L}\left[\boldsymbol{y}(t) - \hat{\boldsymbol{y}}(t)\right] \\ \hat{\boldsymbol{y}}(t) = \boldsymbol{C}\hat{\boldsymbol{x}}(t) \\ \hat{\boldsymbol{z}}(t) = \boldsymbol{H}\hat{\boldsymbol{x}}(t) \end{cases} \tag{8}$$

where $\hat{\boldsymbol{x}}(t)$, $\hat{\boldsymbol{y}}(t)$, $\hat{\boldsymbol{z}}(t)$ are the observation values of $\boldsymbol{x}$, $\boldsymbol{T}_{\text{sensor}}$ and $\boldsymbol{T}_{\text{out}}$, respectively; and $\boldsymbol{y}(t)$ is the vector of sensors measurements. As mentioned above, there are discrepancies ($\Delta\boldsymbol{\theta}$) between the parameters ($\boldsymbol{\theta}^0$) of the thermal model in the observer and the actual parameters ($\boldsymbol{\theta}$), as shown in (9)–(11).

$$\boldsymbol{\theta}^0 = [R_{1\_13} \cdots R_{h162\_8}, C_1 \cdots C_{h162\_8}]^{\mathrm{T}} \tag{9}$$

$$\Delta\boldsymbol{\theta} = [\Delta R_{1\_13} \cdots \Delta R_{h162\_8}, \Delta C_1 \cdots \Delta C_{h162\_8}]^{\mathrm{T}} \tag{10}$$

$$\boldsymbol{\theta} = [\theta_1, \theta_2 \cdots \theta_{Np}]^{\mathrm{T}} = \boldsymbol{\theta}^0 + \Delta\boldsymbol{\theta} \tag{11}$$

The actual parameter $\boldsymbol{\theta}$ is uncertain but bounded, so $\forall \theta_i \in \boldsymbol{\theta}$ can be expressed by:

$$\theta_{i\_\min} \leqslant \theta_i \leqslant \theta_{i\_\max}, \forall \theta_i \in \boldsymbol{\theta} \tag{12}$$

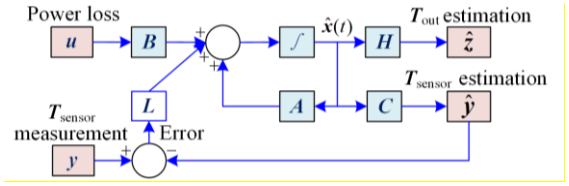


Fig. 10. Proposed 3-D $H_\infty$ temperature observer.

Based on the analysis from [28], [29], and [45], the thermal model parameter uncertainties mainly exist in the thermal resistances ($R_{\text{th}}$) and thermal capacitances ($C_{\text{th}}$) of the DBC solder, baseplate, TIM, heatsink plate layer and convection part. Therefore, the settings for $\theta_{i\_\min}$ and $\theta_{i\_\max}$ are as follows:

1) If $\theta_i$ is an $R_{\text{th}}$ in the DBC solder layer, TIM layer, or convection part, it is set to be bounded in $[0.8\,\theta_i^0, 5\,\theta_i^0]$.

2) If $\theta_i$ is an $R_{\text{th}}$ in other layers, it is bounded in $[0.8\,\theta_i^0, 2.5\,\theta_i^0]$.

3) If $\theta_i$ is a $C_{\text{th}}$ in the above layers, it is bounded within $[0.7\,\theta_i^0, 1.3\,\theta_i^0]$.

It is worth noting that $\theta_{i\_\min}$ and $\theta_{i\_\max}$ can be set according to specific applications and different from those in this paper, while the design and analysis methods are still applicable. Considering the model parameter variations and loss calculation errors, the actual thermal behavior of the IGBT module can be expressed by (13).

$$\begin{cases} \dfrac{\mathrm{d}\boldsymbol{x}(t)}{\mathrm{d}t} = (\boldsymbol{A} + \Delta\boldsymbol{A}(\boldsymbol{\theta}))\boldsymbol{x}(t) + \boldsymbol{B}\boldsymbol{u}(t) + \boldsymbol{D}\boldsymbol{\delta}(t) \\ \boldsymbol{y}(t) = \boldsymbol{C}\boldsymbol{x}(t) \\ \boldsymbol{z}(t) = \boldsymbol{H}\boldsymbol{x}(t) \end{cases} \tag{13}$$

where $\Delta\boldsymbol{A}(\boldsymbol{\theta})$ represents the change in the system matrix $\boldsymbol{A}$ caused by $\Delta\boldsymbol{\theta}$; $\boldsymbol{\delta}(t)$ represents the disturbances including loss calculation errors, deviation of $\boldsymbol{B}$, model truncation error, and the influence of any other factors which were not considered during modeling; $\boldsymbol{D}$ is an identity matrix.

From (8) and (13), the errors of $\boldsymbol{x}$ and $\boldsymbol{T}_{\text{out}}$ can be defined as $\boldsymbol{e}_x(t)$ and $\boldsymbol{e}_z(t)$, respectively, which satisfy the following:

$$\begin{cases} \dfrac{\mathrm{d}\boldsymbol{e}_x(t)}{\mathrm{d}t} = (\boldsymbol{A} - \boldsymbol{L}\boldsymbol{C})\boldsymbol{e}_x(t) + \Delta\boldsymbol{A}(\boldsymbol{\theta})\boldsymbol{x}(t) + \boldsymbol{D}\boldsymbol{\delta}(t) \\ \boldsymbol{e}_z(t) = \boldsymbol{H}\boldsymbol{e}_x(t) \end{cases} \tag{14}$$

As evidenced from (14), due to the presence of $\Delta\boldsymbol{A}(\boldsymbol{\theta})$ and $\boldsymbol{\delta}(t)$, the energy of $\boldsymbol{u}$(t) and $\boldsymbol{\delta}(t)$ are transferred to $\boldsymbol{e}_x(t)$ and $\boldsymbol{e}_z(t)$. Thus, conventional Luenberger observers relying on placing the eigenvalues of $\boldsymbol{A}$-$\boldsymbol{LC}$ in the left half-plane of the complex plane cannot theoretically guarantee $\boldsymbol{e}_x(t)$ and $\boldsymbol{e}_z(t)$ to converge to zero. Consequently, temperature estimation errors are unavoidable. By contrast, the proposed $H_\infty$ observer has temperature estimation robustness to $\Delta\boldsymbol{A}(\boldsymbol{\theta})$ and $\boldsymbol{\delta}(t)$ by effective combination of the thermal model and measurements, which is achieved by the optimal design of the observer feedback gain $\boldsymbol{L}$.

*B. Design of the Feedback Gain* $\boldsymbol{L}$

This subsection details the methodology for the optimal design of the feedback gain $\boldsymbol{L}$. The augmented state and input vectors are defined as:

$$\boldsymbol{\xi}(t)=\begin{bmatrix}\boldsymbol{e}_x(t) & \boldsymbol{x}(t)\end{bmatrix}^{\mathrm{T}} \tag{15}$$

$$\boldsymbol{d}(t)=\begin{bmatrix}\boldsymbol{u}(t) & \boldsymbol{\delta}(t)\end{bmatrix}^{\mathrm{T}} \tag{16}$$

According to (15) and (16), the state space with $\boldsymbol{\xi}(t)$ as the state variable can be represented as:

$$\begin{cases}\dfrac{\mathrm{d}\boldsymbol{\xi}(t)}{\mathrm{d}t}=\boldsymbol{A}_{\mathrm{p}}\boldsymbol{\xi}(t)+\boldsymbol{B}_{\mathrm{p}}\boldsymbol{d}(t)\\ \boldsymbol{e}_z(t)=\boldsymbol{G}_{\mathrm{p}}\boldsymbol{\xi}(t)\end{cases} \tag{17}$$

where $\boldsymbol{e}_z(t)$ is the estimation error of $\boldsymbol{T}_{\mathrm{out}}$, its magnitude is determined by its signal energy; $\boldsymbol{A}_{\mathrm{p}}$, $\boldsymbol{B}_{\mathrm{p}}$ and $\boldsymbol{G}_{\mathrm{p}}$ are defined as follows:

$$\begin{cases}\boldsymbol{A}_{\mathrm{p}}=\begin{bmatrix}\boldsymbol{A}-\boldsymbol{LC} & \Delta\boldsymbol{A}\\ \boldsymbol{0} & \boldsymbol{A}+\Delta\boldsymbol{A}\end{bmatrix}\\ \boldsymbol{B}_{\mathrm{p}}=\begin{bmatrix}\boldsymbol{0} & \boldsymbol{D}\\ \boldsymbol{B} & \boldsymbol{D}\end{bmatrix}\\ \boldsymbol{G}_{\mathrm{p}}=[\boldsymbol{H} \quad \boldsymbol{0}]\end{cases} \tag{18}$$

Therefore, reducing the energy of $\boldsymbol{e}_z(t)$ is the key to improving temperature estimation accuracy. From (17), it is known that $\boldsymbol{e}_z(t)$ derives its energy from $\boldsymbol{d}(t)$. Thus, the goal of the optimal design of $\boldsymbol{L}$ is to suppress the energy transfer from $\boldsymbol{d}(t)$ to $\boldsymbol{e}_z(t)$. To quantitatively assess the attenuation of the energy of $\boldsymbol{e}_z(t)$ relative to that of $\boldsymbol{d}(t)$, the frequency domain transfer function ($\boldsymbol{T}_{\mathrm{ezd}}(\mathrm{j}\omega)$) from $\boldsymbol{d}(\mathrm{j}\omega)$ to $\boldsymbol{e}_z(\mathrm{j}\omega)$ is defined, shown as:

$$\boldsymbol{T}_{\mathrm{ezd}}(\mathrm{j}\omega)=\boldsymbol{G}_{\mathrm{p}}(\mathrm{j}\omega\boldsymbol{I}-\boldsymbol{A}_{\mathrm{p}})^{-1}\boldsymbol{B}_{\mathrm{p}}=\frac{\boldsymbol{e}_z(\mathrm{j}\omega)}{\boldsymbol{d}(\mathrm{j}\omega)} \tag{19}$$

Then, the $H_\infty$ norm of $\boldsymbol{T}_{\mathrm{ezd}}(\mathrm{j}\omega)$, denoted by $\left\|\boldsymbol{T}_{\mathrm{ezd}}(\mathrm{j}\omega)\right\|_\infty$, which is the maximum gain of $\left\|\boldsymbol{e}_z(\mathrm{j}\omega)\right\|_2$ relative to $\left\|\boldsymbol{d}(\mathrm{j}\omega)\right\|_2$ within the frequency range of $\omega\in[0, +\infty)$, is defined as:

$$\left\|\boldsymbol{T}_{\mathrm{ezd}}(\mathrm{j}\omega)\right\|_\infty=\sup_{\omega\in[0,\infty)}\frac{\left\|\boldsymbol{e}_z(\mathrm{j}\omega)\right\|_2}{\left\|\boldsymbol{d}(\mathrm{j}\omega)\right\|_2} \tag{20}$$

Based on $\left\|\boldsymbol{T}_{\mathrm{ezd}}(\mathrm{j}\omega)\right\|_\infty$, the objective function for the design of $\boldsymbol{L}$ is defined in (21), whose core idea is to minimize the energy transferred from $\boldsymbol{d}(t)$ to the estimation error $\boldsymbol{e}_z(t)$ in the worst case by minimizing $\left\|\boldsymbol{T}_{\mathrm{ezd}}(\mathrm{j}\omega)\right\|_\infty$ under all possible cases of parameter uncertainties.

$$\arg\min_{\boldsymbol{L}}\left\|\boldsymbol{T}_{\mathrm{ezd}}(\mathrm{j}\omega)\right\|_\infty,\ \text{s.t. } \theta_{i\_\min}\leqslant\theta_i\leqslant\theta_{i\_\max},\forall\theta_i\in\boldsymbol{\theta} \tag{21}$$

Because $\Delta\boldsymbol{A}$ is infeasible to obtain, a crucial challenge in solving the optimization problem for the $\boldsymbol{L}$ in (21) is its dependence on $\Delta\boldsymbol{A}$. To overcome this limitation, the uncertainty matrix denoted by $\boldsymbol{E}_A$ is defined in (22), while $\Delta\boldsymbol{A}$ can then be expressed as a scaled version of $\boldsymbol{E}_A$ as shown in (23).

$$\begin{cases}\boldsymbol{E}_A(i,j)=\arg\max_{\boldsymbol{\theta}}\left|\Delta\boldsymbol{A}(i,j)\right|,\ i,\ j\in\{1,2\cdots n\},\\ \text{s.t. } \theta_{i\_\min}\leqslant\theta_i\leqslant\theta_{i\_\max},\forall\theta_i\in\boldsymbol{\theta}\end{cases} \tag{22}$$

$$\Delta\boldsymbol{A}=\boldsymbol{E}_A\sum\nolimits_A(t)\boldsymbol{F}_A \tag{23}$$

where $\boldsymbol{F}_A=\boldsymbol{I}_n$; $\sum_A(t)$ is a Lebesgue measurable function and satisfies $\left\|\sum_A(t)\right\|\leqslant 1$, and $\sum_A(t)$ is chosen as a real scalar in this paper. Subsequently, the optimal $\boldsymbol{L}$ of the proposed observer with the goal in (21) can be solved according to Theorem 1.

**Theorem 1:** If the feedback gain $\boldsymbol{L}$ satisfies the matrix inequality in (24), the system in (17) is asymptotically stable and satisfies $\left\|\boldsymbol{T}_{\mathrm{ezd}}(\mathrm{j}\omega)\right\|_\infty<\gamma$. In (24), $\gamma$, $\varepsilon_1$, and $\varepsilon_2$ are scalars and satisfy $\gamma>0$, $\varepsilon_1>0$, and $\varepsilon_2>0$; $\boldsymbol{P}_1$ and $\boldsymbol{P}_2$ are symmetric positive definite matrices; $\boldsymbol{G}_1=\boldsymbol{H}^{\mathrm{T}}$; $\boldsymbol{G}_2=\boldsymbol{0}$; and * denotes the symmetric elements of the matrix. Therefore, by treating $\gamma$, $\varepsilon_1$, $\varepsilon_2$, $\boldsymbol{P}_1$, $\boldsymbol{P}_2$, and $\boldsymbol{L}$ as unknown variables and solving the matrix inequality in (24), the minimum $\gamma$ and the corresponding optimal $\boldsymbol{L}$ can be obtained. The obtained $\boldsymbol{L}$ minimizes the worst-case temperature estimation error ($\boldsymbol{e}_z(t)$).

The matrix inequality in (24) can be solved by using Matlab's linear matrix inequality (LMI) toolbox. The proof of Theorem 1 is given in Appendix A.

$$\begin{bmatrix}\boldsymbol{P}_1(\boldsymbol{A}-\boldsymbol{LC})+(\boldsymbol{A}-\boldsymbol{LC})^{\mathrm{T}}\boldsymbol{P}_1 & \boldsymbol{0} & \boldsymbol{0} & \boldsymbol{P}_1\boldsymbol{D} & \boldsymbol{G}_1 & \boldsymbol{P}_1\boldsymbol{E}_A & \boldsymbol{0}\\ * & \boldsymbol{P}_2\boldsymbol{A}+\boldsymbol{A}^{\mathrm{T}}\boldsymbol{P}_2+(\varepsilon_1+\varepsilon_2)\boldsymbol{F}_A{}^{\mathrm{T}}\boldsymbol{F}_A & \boldsymbol{P}_2\boldsymbol{B} & \boldsymbol{P}_2\boldsymbol{D} & \boldsymbol{G}_2 & \boldsymbol{0} & \boldsymbol{P}_2\boldsymbol{E}_A\\ * & * & -\gamma\boldsymbol{I} & \boldsymbol{0} & \boldsymbol{0} & \boldsymbol{0} & \boldsymbol{0}\\ * & * & * & -\gamma\boldsymbol{I} & \boldsymbol{0} & \boldsymbol{0} & \boldsymbol{0}\\ * & * & * & * & -\gamma\boldsymbol{I} & \boldsymbol{0} & \boldsymbol{0}\\ * & * & * & * & * & -\varepsilon_1\boldsymbol{I} & \boldsymbol{0}\\ * & * & * & * & * & * & -\varepsilon_2\boldsymbol{I}\end{bmatrix}<0 \tag{24}$$

## IV. EXPERIMENTS

In the following section, the proposed thermal observer is evaluated experimentally. The experimental setup is introduced first, and experimental results are then presented.

*A. Experiment Setup*

The 1700 V/450 A 2MBI450VN-170 IGBT module is selected as the device under test (DUT). The schematic diagram of the experiment platform is shown in Fig. 11, where circuit topology A and B are used to

evaluate the observer performance under quasi-DC and AC active load conditions, respectively.

The thermal model parameters ($\boldsymbol{\theta}_0$) used in the observer are intentionally altered with respect to the actual parameters ($\boldsymbol{\theta}$) of the DUT, leading to parameter uncertainty while avoiding long-term aging cycles. An additional term $\Delta P$ added into $P$ represents power loss calculation errors. The load current, control signal, and temperature measurements are sampled at 1 kHz and stored in the controller before transmitted to a PC for further processing. The loss calculations and temperature observer are implemented in Matlab/Simulink on the PC with a 1 ms step size.

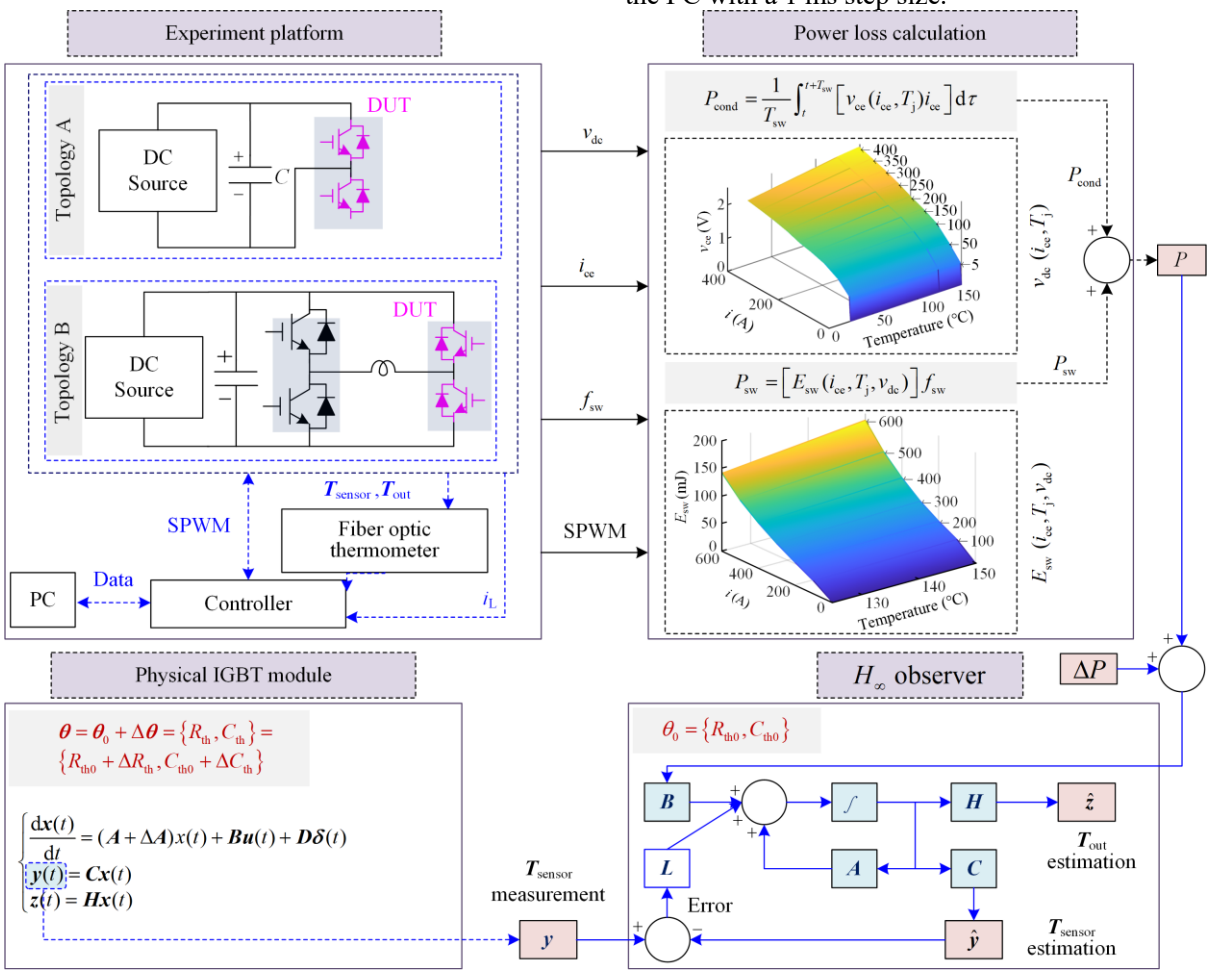


Fig. 11. Schematic diagram of the experiment platform.

Figure 12 presents a photograph of the experiment platform, while Fig. 13 illustrates the specific placement of the temperature sensors. Sensor1 to Sensor3 are all fiber optic temperature sensors (OTG), with a measurement accuracy of 0.05 ℃. Temperature signals can be converted to 0–5 V voltage signals through the DAC of the Opsens fiber optic thermometer. Thermocouples or RTDs can replace the OTG for cost-effective alternatives in practice. The temperatures of the IGBT chip ($T_{HB2}$) and the diode chip ($D_{HB1}$) are measured using the same type of OTG to validate the observer. The performance of the proposed $H_\infty$ observer is compared with two conventional observers: the Luenberger observer (L-observer) based on pole placement and the Kalman filter (KF). In the experiments, the observer gain of the L-observer is designed to ensure the eigenvalue of $\boldsymbol{A}$-$\boldsymbol{LC}$ with the maximum real part is far away from the imaginary axis than the system's eigenvalue with the minimum real part. The process and measurement noise covariance matrix of the KF are determined by trial and error.

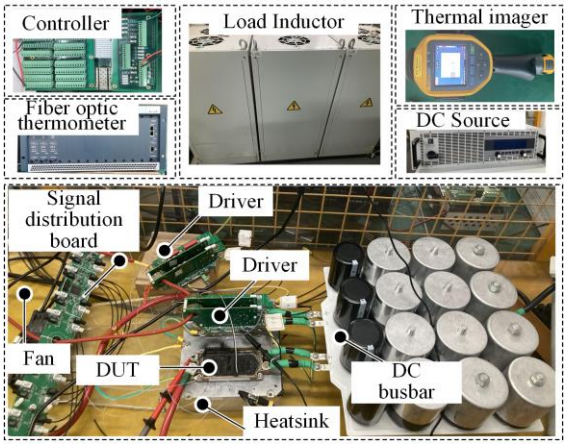


Fig. 12. Physical diagram of the experimental platform.

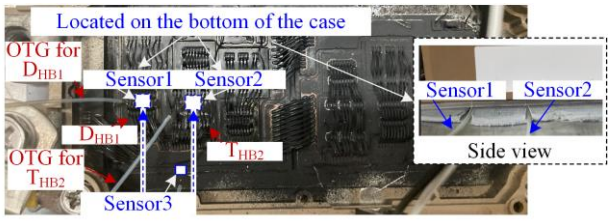


Fig. 13. Sensor locations in the experiment.

Comparative experiments are carried out under Cases 1–8. In each case, the altered parameters $\boldsymbol{\theta}^0$ and the loss error $\Delta P$ with respect to the actual values are set according to Table III. In Table III, $R_{\text{th}0}$ and $C_{\text{th}0}$ denote the thermal resistance and capacitance of the thermal model in the observer, while $R_{\text{th}}$ and $C_{\text{th}}$ represent the actual parameters of the DUT. $P_{\text{TLB}}$, $P_{\text{DLB}}$, $P_{\text{THB}}$, and $P_{\text{DHB}}$ are the actual power losses. In Cases 1–4, the thermal model parameters of DBC solder, baseplate, TIM, heat sink plate, and convection part differ from the actual values, while $\Delta P = 0$. In Cases 5–8, both $\Delta P$ and the deviation of thermal model parameters are under consideration.

TABLE III
ALTERED THERMAL PARAMETERS AND POWER LOSS WITH RESPECT TO ACTUAL VALUES FOR CASES 1–8

| Case | DBC solder | | Baseplate | | TIM layer | | Plate of heatsink | | Convection | | Loss error $\frac{\Delta P}{P}$ | | | |
|---|---|---|---|---|---|---|---|---|---|---|---|---|---|---|
| | $\frac{R_{\text{th}}}{R_{\text{th}0}}$ | $\frac{C_{\text{th}}}{C_{\text{th}0}}$ | $\frac{R_{\text{th}}}{R_{\text{th}0}}$ | $\frac{C_{\text{th}}}{C_{\text{th}0}}$ | $\frac{R_{\text{th}}}{R_{\text{th}0}}$ | $\frac{C_{\text{th}}}{C_{\text{th}0}}$ | $\frac{R_{\text{th}}}{R_{\text{th}0}}$ | $\frac{C_{\text{th}}}{C_{\text{th}0}}$ | $\frac{R_{\text{th}}}{R_{\text{th}0}}$ | $\frac{C_{\text{th}}}{C_{\text{th}0}}$ | $P_{\text{T\_LB}}$ | $P_{\text{D\_LB}}$ | $P_{\text{T\_HB}}$ | $P_{\text{D\_HB}}$ |
| 1 | 0.9 | 1 | 0.95 | 1.05 | 0.93 | 1.08 | 0.88 | 1.14 | 5 | 1 | 0 | 0 | 0 | 0 |
| 2 | 1 | 1 | 0.95 | 1.18 | 5 | 1.05 | 0.95 | 1.05 | 0.97 | 1 | 0 | 0 | 0 | 0 |
| 3 | 4 | 0.77 | 1.5 | 0.8 | 2 | 0.83 | 1.7 | 0.77 | 1.27 | 0.97 | 0 | 0 | 0 | 0 |
| 4 | 1.9 | 0.7 | 2.5 | 0.7 | 1.55 | 0.7 | 2.5 | 0.7 | 1.5 | 0.7 | 0 | 0 | 0 | 0 |
| 5 | 0.9 | 1 | 0.95 | 1.05 | 0.93 | 1.08 | 0.88 | 1.14 | 5 | 1 | −0.32 | 0.38 | −0.32 | 0.38 |
| 6 | 1 | 1 | 0.95 | 1.18 | 5 | 1.05 | 0.95 | 1.05 | 0.97 | 1 | −0.3 | −0.3 | −0.3 | −0.3 |
| 7 | 4 | 0.77 | 1.5 | 0.8 | 2 | 0.83 | 1.7 | 0.77 | 1.27 | 0.97 | 0.06 | 0.06 | 0.06 | 0.06 |
| 8 | 1.9 | 0.7 | 2.5 | 0.7 | 1.55 | 0.7 | 2.5 | 0.7 | 1.5 | 0.7 | 1 | 1.5 | 1 | 1.5 |

*B. Experiment Results*

Experiments are conducted using two topologies to assess the proposed observer's performance and robustness. First, Topology A is employed under DC loss condition for Cases 1–4, as outlined in Table III, which decouples the impact of power loss error, allowing for the evaluation of the observer's robustness to model parameter uncertainties. Subsequently, the observer's robustness to both model parameter and power loss uncertainties is validated using Topology B (single-phase H-bridge) under active load AC condition, as in the settings of Cases 5–8 in Table III. The experimental results are presented and discussed in the following subsections.

*1) Evaluation of Observers Under DC Loss with* $\Delta P = 0$ W

The conduction loss can be calculated precisely using the conduction voltage and current. Thus, in the first set of experiments under DC loss condition for Cases 1–4, $\Delta P$ can be set to be 0, and only model parameter uncertainty is considered. To generate varying levels of conduction losses, a periodic current is applied to the $\text{T}_{\text{HB}}$ chips: (0 A, 50 A, 100 A, 0 A, 50 A, 100 A). A Fluke thermal imager (IR) equipment is employed to cross-verify the temperatures recorded by the OTG sensors, as shown in Fig. 14.

Figures 15–18 illustrate the junction temperature estimates of $\text{T}_{\text{HB2}}$ and $\text{D}_{\text{HB1}}$ by the observers and open-loop thermal model under Cases 1–4.

At $t = 150$ s, the temperature reaches its maximum value. Therefore, the absolute value of the temperature estimation error at this moment, denoted as $A_{E150}$, is used as the metric to evaluate the observers' performance under the DC loss condition, shown as:

$$A_{E150} = |T_{\text{measurement}}(t_0) - T_{\text{estimation}}(t_0)|, t_0 = 150\text{ s} \quad (25)$$

The $AE_{150}$ for $\text{T}_{\text{HB2}}$ and $\text{D}_{\text{HB1}}$ are presented in Fig. 19, Table IV, and Table V, respectively.

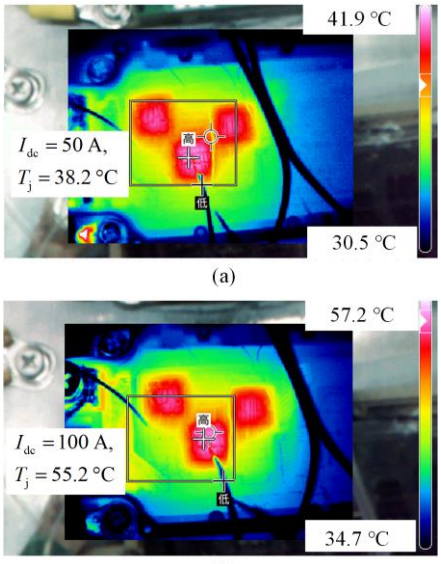


Fig. 14. Cross-verification of $T_{\text{j}}$ with IR imager under DC loss. (a) $I_{\text{dc}} = 50$ A. (b) $I_{\text{dc}} = 100$ A.

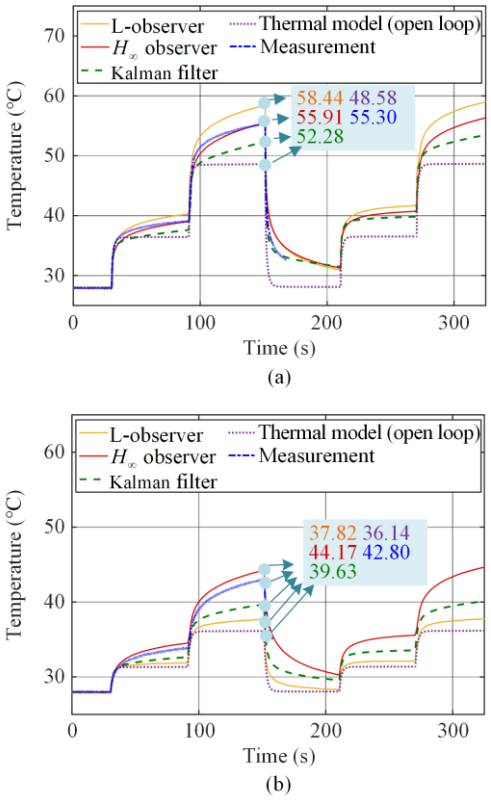


Fig. 15. Temperature estimation under DC loss in Case 1. (a) IGBT ($T_{HB2}$). (b) Diode ($D_{HB1}$).

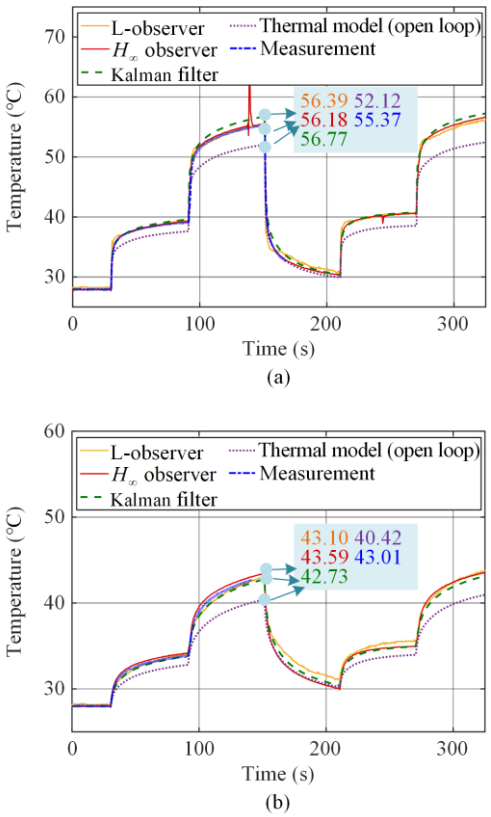


Fig. 16. Temperature estimation under DC loss in Case 2. (a) IGBT ($T_{HB2}$). (b) Diode ($D_{HB1}$).

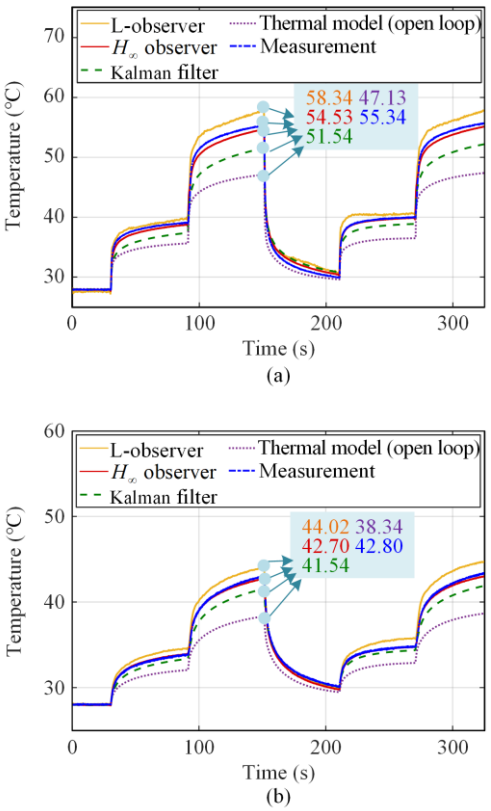


Fig. 17. Temperature estimation under DC loss in Case 3. (a) IGBT ($T_{HB2}$). (b) Diode ($D_{HB1}$).

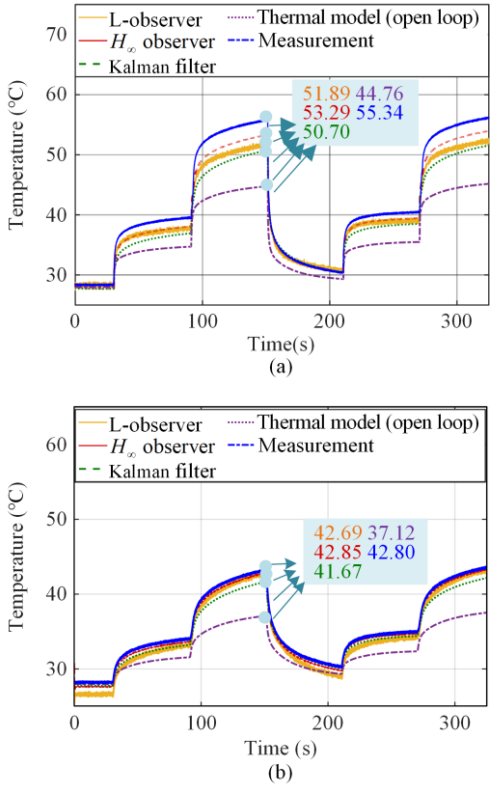


Fig. 18. Temperature estimation under DC loss in Case 4. (a) IGBT ($T_{HB2}$). (b) Diode ($D_{HB1}$).

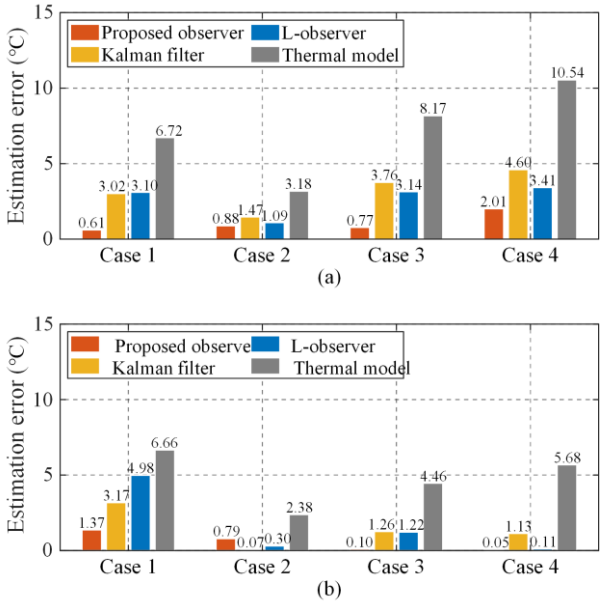


Fig. 19. Temperature estimation errors in Cases 1–4 under DC loss. (a) $A_{E150}$ of IGBT ($T_{HB2}$). (b) $A_{E150}$ of Diode ($D_{HB1}$).

As shown in Table IV, for $T_{HB2}$, the proposed $H_\infty$ observer achieves the highest temperature estimation accuracy in all cases. The maximum $A_{E150}$ values of the proposed observer, KF, and L-observer are 2.01 °C, 4.6 °C, and 3.41 °C, respectively. This is because KF and L-observer cannot theoretically guarantee temperature estimation accuracy when there are model parameter deviations with unknown statistical characteristics. However, the proposed observer is robust to such parameter uncertainties by suppressing the energy transferred from $\boldsymbol{d}(t)$ to estimation error $\boldsymbol{e}_z(t)$. As for the open-loop thermal model, its performance is significantly worse than those of the above three observers due to the lack of feedback correction. Its temperature estimation error for $T_{HB2}$ has a minimum of 3.18 °C and a maximum of 10.54 °C.

TABLE IV
TEMPERATURE ESTIMATION ERRORS OF $T_{HB2}$ UNDER DC LOSS

| Case | Proposed observer (°C) | Kalman filter (°C) | L-observer (°C) | Thermal model (°C) |
|---|---|---|---|---|
| 1 | 0.61 | 3.02 | 3.10 | 6.72 |
| 2 | 0.88 | 1.47 | 1.09 | 3.18 |
| 3 | 0.77 | 3.76 | 3.14 | 8.17 |
| 4 | 2.01 | 4.6 | 3.41 | 10.54 |

TABLE V
TEMPERATURE ESTIMATION ERRORS OF $D_{HB1}$ UNDER DC LOSS

| Case | Proposed observer (°C) | Kalman filter (°C) | L-observer (°C) | Thermal model (°C) |
|---|---|---|---|---|
| 1 | 1.37 | 3.17 | 4.98 | 6.66 |
| 2 | 0.79 | 0.07 | 0.30 | 2.38 |
| 3 | 0.10 | 1.26 | 1.22 | 4.46 |
| 4 | 0.05 | 1.13 | 0.11 | 5.68 |

Similar results are obtained for the temperature estimation of $D_{HB1}$, as shown in Table V. Among the four methods in Table V, the proposed $H_\infty$ observer achieves the best performance in Cases 1, 3, and 4. Although in Case 2, KF has the lowest $A_{E150}$ of 0.07 °C, the proposed observer's maximum $A_{E150}$ across all cases is only 1.37 °C, significantly lower than the maximum $A_{E150}$ of KF (3.17 °C) and L-observer (4.98 °C).

The above results demonstrate that compared to the L-observer and KF, the $H_\infty$ observer has stronger robustness to parameter uncertainties when the power loss is accurately calculated.

*2) Evaluation of Observers Under* AC *Active Load Condition with* $\Delta P \neq 0$ W

The robustness of the proposed observer is further validated in the second set of experiments with AC active load (Cases 5 to 8 in Table III), where both the model parameters and power losses are subjected to errors. Figures 20–23 illustrate the estimations of the junction temperatures of $T_{HB2}$ and $D_{HB1}$ by the proposed $H_\infty$ observer, L-observer, KF, and open-loop thermal model under Cases 5–8 when the amplitude of the load current is 140 A, and the switching frequency is 2 kHz.

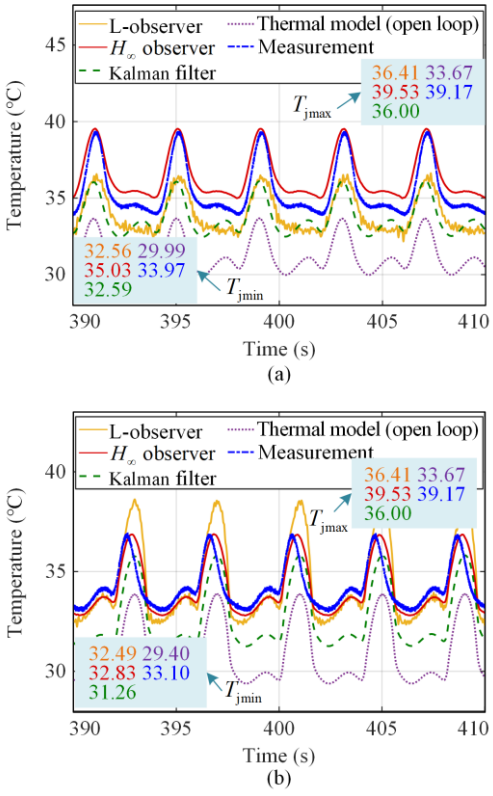


Fig. 20. Temperature estimation under AC active load in Case 5. (a) IGBT ($T_{HB2}$). (b) Diode ($D_{HB1}$).

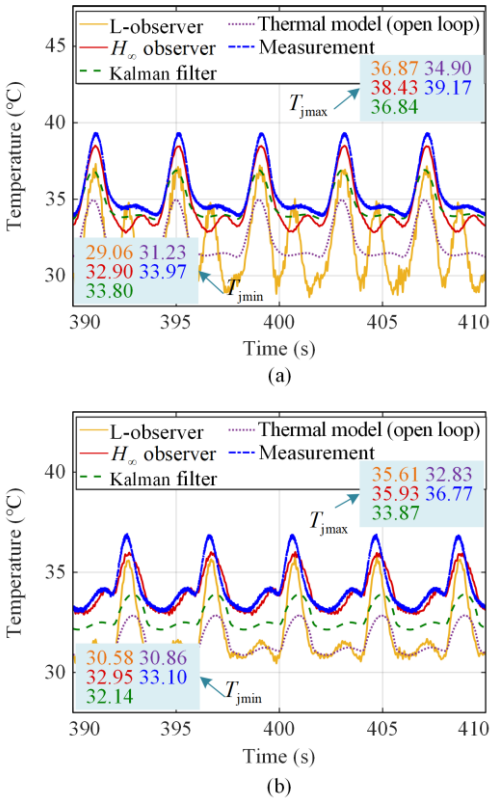


Fig. 21. Temperature estimation under AC active load in Case 6. (a) IGBT ($T_{HB2}$). (b) Diode ($D_{HB1}$).

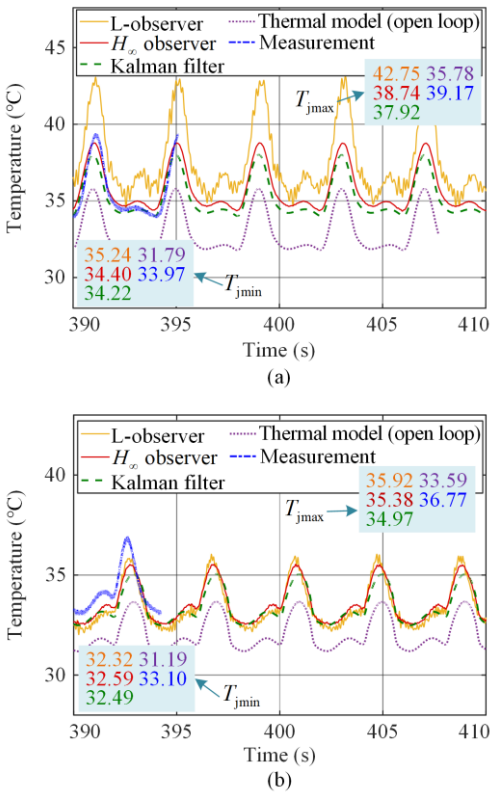


Fig. 22. Temperature estimation under AC active load in Case 7. (a) IGBT ($T_{HB2}$). (b) Diode ($D_{HB1}$).

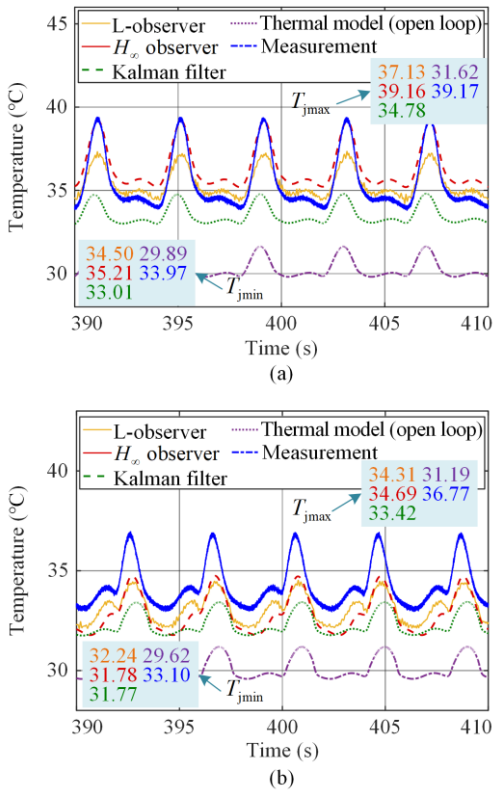


Fig. 23. Temperature estimation under AC active load in Case 8. (a) IGBT ($T_{HB2}$). (b) Diode ($D_{HB1}$).

Let $T_{jmax}$ and $\Delta T_j$ represent the maximum junction temperature and the temperature swings, respectively. The errors of $T_{jmax}$ and $\Delta T_j$ are presented in Fig. 24 and Table VI.

Similar to the cases with only parameter uncertainties, it can be seen that the proposed observer outperforms the KF, L-observer, and open-loop thermal model. Specifically, in Cases 5–8, the estimation errors of $T_{jmax}$ and $\Delta T_j$ of $T_{HB2}$ under the proposed observer are the smallest, whereas in Cases 5, 6, and 8, the proposed observer has the highest estimation accuracies for $T_{jmax}$ and $\Delta T_j$ of $D_{HB1}$. In addition to achieving the highest estimation accuracies in most cases, the proposed observer also performs best in terms of maximum estimation error. In Cases 5 to 8, for $T_{HB2}$, the maximum estimation errors of $T_{jmax}$ for the proposed observer, KF, L-observer, and open-loop thermal model are 0.74 °C, 4.39 °C, 3.58 °C, and 7.55 °C, respectively, while the maximum estimation errors of $\Delta T_j$ are 1.25 °C, 3.43 °C, 2.61 °C, and 3.47 °C, respectively. For $D_{HB1}$, the maximum errors of $T_{jmax}$ for the proposed observer, KF, L-observer, and open-loop thermal model are 2.08 °C, 3.35 °C, 2.46 °C, and 5.58 °C, respectively, whereas the maximum estimation errors of $\Delta T_j$ are 0.76 °C, 2.02 °C, 2.40 °C, and 2.10 °C, respectively.

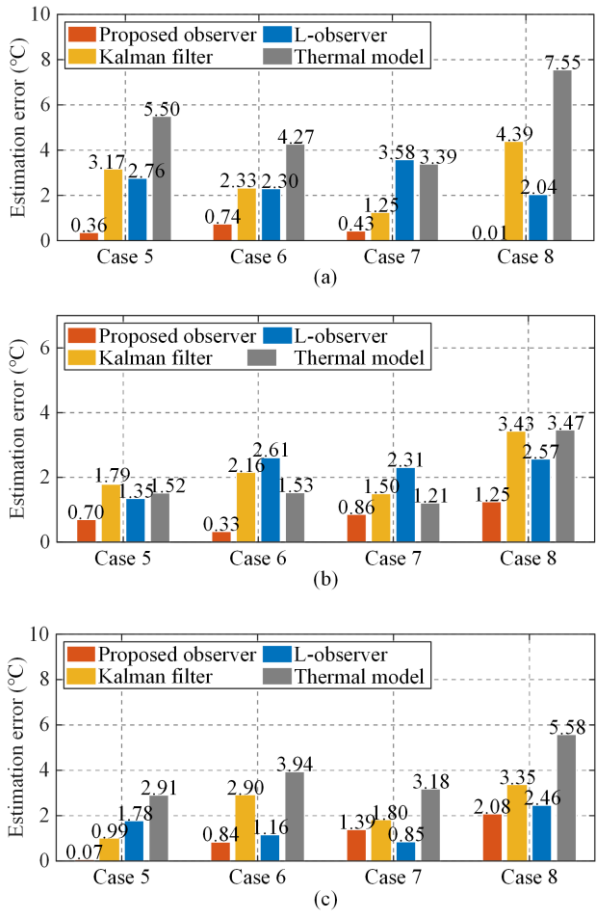


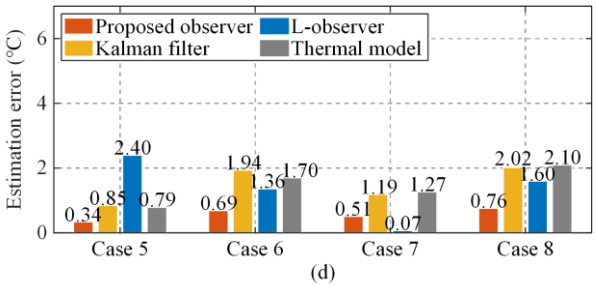


Fig. 24. Temperature estimation errors in Cases 5–8 under AC active load. (a) $T_{jmax}$ estimation errors of IGBT ( $T_{HB2}$ ). (b) $\Delta T_j$ estimation errors of IGBT ( $T_{HB2}$ ). (c) $T_{jmax}$ estimation errors of diode ( $D_{HB1}$ ). (d) $\Delta T_j$ estimation errors of diode ( $D_{HB1}$ ).

In summary, in Cases 5–8, the proposed method reduces the sum of estimation errors for the IGBT's $T_{jmax}$ by 86.18%, 85.58%, and 92.56% compared to the Kalman filter, L-observer, and open-loop thermal model, respectively. For the sum of estimation errors of the IGBT's $\Delta T_j$, the reductions are 64.64%, 64.48%, and 59.38%, respectively. Regarding the sum of estimation errors for the diode's $T_{jmax}$ in Cases 5 to 8, the proposed method achieves reductions of 47.98%, 29.92%, and 71.94%, respectively. Finally, for the sum of estimation errors of the diode's $\Delta T_j$, the reductions are 61.67%, 57.64%, and 60.75%, respectively.

TABLE VI
TEMPERATURE ESTIMATION ERRORS OF $T_{HB2}$ AND $D_{HB1}$ UNDER AC ACTIVE LOAD

| | | | Proposed observer (℃) | Kalman filter (℃) | L-observer (℃) | Thermal model (℃) |
|---|---|---|---|---|---|---|
| $T_{HB2}$ | Case 5 | $T_{jmax}$ | 0.36 | 3.17 | 2.76 | 5.50 |
| | | $\Delta T_j$ | 0.70 | 1.79 | 1.35 | 1.52 |
| | Case 6 | $T_{jmax}$ | 0.74 | 2.33 | 2.30 | 4.27 |
| | | $\Delta T_j$ | 0.33 | 2.16 | 2.61 | 1.53 |
| | Case 7 | $T_{jmax}$ | 0.43 | 1.25 | 3.58 | 3.39 |
| | | $\Delta T_j$ | 0.86 | 1.50 | 2.31 | 1.21 |
| | Case 8 | $T_{jmax}$ | 0.01 | 4.39 | 2.04 | 7.55 |
| | | $\Delta T_j$ | 1.25 | 3.43 | 2.57 | 3.47 |
| $D_{HB1}$ | Case 5 | $T_{jmax}$ | 0.07 | 0.99 | 1.78 | 2.91 |
| | | $\Delta T_j$ | 0.34 | 0.85 | 2.40 | 0.79 |
| | Case 6 | $T_{jmax}$ | 0.84 | 2.90 | 1.16 | 3.94 |
| | | $\Delta T_j$ | 0.69 ℃ | 1.94 | 1.36 | 1.70 |
| | Case 7 | $T_{jmax}$ | 1.39 | 1.80 | 0.85 | 3.18 |
| | | $\Delta T_j$ | 0.51 | 1.19 | 0.07 | 1.27 |
| | Case 8 | $T_{jmax}$ | 2.08 | 3.35 | 2.46 | 5.58 |
| | | $\Delta T_j$ | 0.76 | 2.02 | 1.60 | 2.10 |

It is worth noting that Kalman filters and Luenberger observers perform even worse than the open-loop thermal model in some cases due to the lack of robustness against system uncertainties with unknown statistical characteristics. For instance, in Case 7, for $T_{\mathrm{jmax}}$ and $\Delta T_{\mathrm{j}}$ of $\mathrm{T_{HB2}}$, the open-loop thermal model has estimation errors of 3.39 ℃ and 1.21 ℃, compared to 3.58 ℃ and 2.31 ℃ with the L-observer. Additionally, in Case 5, the L-observer's $\Delta T_{\mathrm{j}}$ estimation error for $\mathrm{D_{HB1}}$ is 2.40 ℃, larger than the 0.79 ℃ from the open-loop thermal model. The KF's estimation accuracy also exhibits similar instability. For instance, in Case 5, the $\Delta T_{\mathrm{j}}$ estimation error of KF for $\mathrm{T_{HB2}}$ is 1.79 ℃, larger than the 1.52 ℃ from the open-loop thermal model. In contrast, the temperature estimation accuracy of the proposed observer is significantly higher than the open-loop thermal model in all Cases.

Results further verify that, as the robustness to system uncertainties can be theoretically guaranteed, the proposed method can achieve higher temperature estimation accuracy for IGBT modules even with power loss and thermal model parameter errors.

### *C. Time Cost of Proposed Method*

The overall time consumption of the FEM model, open loop thermal model, and thermal observers are analyzed in Table VII when using Intel i9 13900H CPU with 32-GB RAM running Windows 11. For a simulation duration of 1 s and solving step of 1 ms, the time cost of the FEM model is $1.08\times10^{6}$ s, whereas the time consumption of the proposed method is only $1.21\times10^{-2}$ s, due to the benefit brought by the model reduction technique.

TABLE VII
TIME COSTS WITH EACH METHODS

| Method | Numerical integration method | Time cost (s) |
|---|---|---|
| FEM model | | $1.08\times10^{6}$ |
| Thermal model | Backward Euler | $1.10\times10^{-2}$ |
| $H_\infty$ observer | Backward Euler | $1.21\times10^{-2}$ |
| Kalman filter | Backward Euler | $1.46\times10^{-2}$ |
| L-observer | Backward Euler | $1.19\times10^{-2}$ |

## V. CONCLUSION

By combining the $H_\infty$ observer with a 3-D reduced-order thermal model of IGBT modules for the first time, a robust, real-time 3-D temperature monitoring method for IGBT modules is proposed in this paper, which can achieve satisfactory temperature estimation accuracy even with thermal model parameter and power loss calculation errors. The main work and key contributions are summarized as follows:

1) A reduced-order 3-D thermal model (ROM) for IGBT modules derived from FEM simulation and model reduction technology is provided. The ROM can estimate IGBT temperatures with errors less than 3% compared to FEM simulation and can be used for real-time thermal monitoring with high computational efficiency.

2) Based on the ROM, by modeling the thermal model parameter variations and power loss calculation errors as the respective uncertain coefficient matrices in the state-space and disturbance, and by minimizing the $H_\infty$ norm of the transfer function from disturbances to temperature estimation errors, the observer's feedback gain is optimally designed. The thermal model is effectively fused with temperature measurements and estimation errors in the worst case are minimized. As a result, the robustness of the temperature estimation to system uncertainties is theoretically guaranteed.

3) Comparative experimental results in multiple cases show that, with thermal parameter and power loss errors, the proposed method can reduce the maximum junction temperature estimation error of IGBT by 85.58% and achieves the highest estimation accuracy in 87.50% of the cases, compared to existing temperature observers for IGBT modules.

Therefore, the proposed method can effectively enhance the reliability of condition monitoring for high-power IGBT modules throughout their whole lifecycle.

## APPENDIX A

In the proof of Theorem1, the following Lemma1 is used.

**Lemma1:** Let $\boldsymbol{E}$ and $\boldsymbol{F}$ be the constant matrices and $\varepsilon$ be an arbitrary positive scalar. For any matrix $\sum(t)$ satisfying $\sum^{\mathrm{T}}(t)\sum(t)\leqslant\boldsymbol{I}$, there is:

$$\boldsymbol{E}\sum(t)\boldsymbol{F}+(\boldsymbol{E}\sum(t)\boldsymbol{F})^{\mathrm{T}}\leqslant\varepsilon^{-1}\boldsymbol{E}\boldsymbol{E}^{\mathrm{T}}+\varepsilon\boldsymbol{F}^{\mathrm{T}}\boldsymbol{F} \tag{A1}$$

**Proof of Theorem1**: By the bounded real lemma [46], when inequality (A2) holds, the system in (17) is asymptotically stable and satisfies $\left\|\boldsymbol{T}_{\mathrm{ezd}}(\mathrm{j}\omega)\right\|_\infty<\gamma$.

$$\begin{cases}\boldsymbol{I}_{\mathrm{LMI1}}=\begin{bmatrix}\boldsymbol{P}\boldsymbol{A}_{\mathrm{p}}+\boldsymbol{A}_{\mathrm{p}}^{\mathrm{T}}\boldsymbol{P} & \boldsymbol{P}\boldsymbol{B}_{\mathrm{p}} & \boldsymbol{G}_{\mathrm{p}}^{\mathrm{T}}\\ * & -\gamma\boldsymbol{I} & \boldsymbol{0}\\ * & * & -\gamma\boldsymbol{I}\end{bmatrix}<0\\ \boldsymbol{P}=\begin{bmatrix}\boldsymbol{P}_1 & \boldsymbol{0}\\ \boldsymbol{0} & \boldsymbol{P}_2\end{bmatrix}\end{cases} \tag{A2}$$

$$\begin{aligned}\boldsymbol{I}_{\mathrm{LMI1}}=&\begin{bmatrix}\boldsymbol{P}_1(\boldsymbol{A}-\boldsymbol{LC})+(\boldsymbol{A}-\boldsymbol{LC})^{\mathrm{T}}\boldsymbol{P}_1 & \boldsymbol{0} & \boldsymbol{0} & \boldsymbol{P}_1\boldsymbol{D} & \boldsymbol{G}_1\\ * & \boldsymbol{P}_2\boldsymbol{A}+\boldsymbol{A}^{\mathrm{T}}\boldsymbol{P}_2 & \boldsymbol{P}_2\boldsymbol{B} & \boldsymbol{P}_2\boldsymbol{D} & \boldsymbol{G}_2\\ * & * & -\gamma\boldsymbol{I} & \boldsymbol{0} & \boldsymbol{0}\\ * & * & * & -\gamma\boldsymbol{I} & \boldsymbol{0}\\ * & * & * & * & -\gamma\boldsymbol{I}\end{bmatrix}+\begin{bmatrix}\boldsymbol{P}_1\boldsymbol{E}_A\\ \boldsymbol{0}\\ \boldsymbol{0}\\ \boldsymbol{0}\\ \boldsymbol{0}\end{bmatrix}\sum\nolimits_A\begin{bmatrix}\boldsymbol{0} & \boldsymbol{F}_A & \boldsymbol{0} & \boldsymbol{0} & \boldsymbol{0}\end{bmatrix}+\\ &\begin{bmatrix}\boldsymbol{0}\\ \boldsymbol{F}_A^{\mathrm{T}}\\ \boldsymbol{0}\\ \boldsymbol{0}\\ \boldsymbol{0}\end{bmatrix}\sum\nolimits_A^{\mathrm{T}}\begin{bmatrix}\boldsymbol{E}_A^{\mathrm{T}}\boldsymbol{P}_1 & \boldsymbol{0} & \boldsymbol{0} & \boldsymbol{0} & \boldsymbol{0}\end{bmatrix}+\begin{bmatrix}\boldsymbol{0}\\ \boldsymbol{P}_2\boldsymbol{E}_A\\ \boldsymbol{0}\\ \boldsymbol{0}\\ \boldsymbol{0}\end{bmatrix}\sum\nolimits_A\begin{bmatrix}\boldsymbol{0} & \boldsymbol{F}_A & \boldsymbol{0} & \boldsymbol{0} & \boldsymbol{0}\end{bmatrix}+\begin{bmatrix}\boldsymbol{0}\\ \boldsymbol{F}_A^{\mathrm{T}}\\ \boldsymbol{0}\\ \boldsymbol{0}\\ \boldsymbol{0}\end{bmatrix}\sum\nolimits_A^{\mathrm{T}}\begin{bmatrix}\boldsymbol{0} & \boldsymbol{E}_A^{\mathrm{T}}\boldsymbol{P}_2 & \boldsymbol{0} & \boldsymbol{0} & \boldsymbol{0}\end{bmatrix}\end{aligned} \tag{A3}$$

$$\begin{aligned}\boldsymbol{I}_{\mathrm{LMI1}}\leqslant\boldsymbol{I}_{\mathrm{LMI2}}=&\begin{bmatrix}\boldsymbol{P}_1(\boldsymbol{A}-\boldsymbol{LC})+(\boldsymbol{A}-\boldsymbol{LC})^{\mathrm{T}}\boldsymbol{P}_1 & \boldsymbol{0} & \boldsymbol{0} & \boldsymbol{P}_1\boldsymbol{D} & \boldsymbol{G}_1\\ * & \boldsymbol{P}_2\boldsymbol{A}+\boldsymbol{A}^{\mathrm{T}}\boldsymbol{P}_2+(\varepsilon_1+\varepsilon_2)\boldsymbol{F}_A^{\mathrm{T}}\boldsymbol{F}_A & \boldsymbol{P}_2\boldsymbol{B} & \boldsymbol{P}_2\boldsymbol{D} & \boldsymbol{G}_2\\ * & * & -\gamma\boldsymbol{I} & \boldsymbol{0} & \boldsymbol{0}\\ * & * & * & -\gamma\boldsymbol{I} & \boldsymbol{0}\\ * & * & * & * & -\gamma\boldsymbol{I}\end{bmatrix}+\\ &\varepsilon_1^{-1}\begin{bmatrix}\boldsymbol{P}_1\boldsymbol{E}_A\\ \boldsymbol{0}\\ \boldsymbol{0}\\ \boldsymbol{0}\\ \boldsymbol{0}\end{bmatrix}\begin{bmatrix}\boldsymbol{E}_A^{\mathrm{T}}\boldsymbol{P}_1 & \boldsymbol{0} & \boldsymbol{0} & \boldsymbol{0} & \boldsymbol{0}\end{bmatrix}+\varepsilon_2^{-1}\begin{bmatrix}\boldsymbol{0}\\ \boldsymbol{P}_2\boldsymbol{E}_A\\ \boldsymbol{0}\\ \boldsymbol{0}\\ \boldsymbol{0}\end{bmatrix}\begin{bmatrix}\boldsymbol{0} & \boldsymbol{E}_A^{\mathrm{T}}\boldsymbol{P}_2 & \boldsymbol{0} & \boldsymbol{0} & \boldsymbol{0}\end{bmatrix}\end{aligned} \tag{A4}$$

$$\begin{cases}\boldsymbol{S}_{11}=\begin{bmatrix}\boldsymbol{P}_1(\boldsymbol{A}-\boldsymbol{LC})+(\boldsymbol{A}-\boldsymbol{LC})^{\mathrm{T}}\boldsymbol{P}_1 & \boldsymbol{0} & \boldsymbol{0} & \boldsymbol{P}_1\boldsymbol{D} & \boldsymbol{G}_1\\ * & \boldsymbol{P}_2\boldsymbol{A}+\boldsymbol{A}^{\mathrm{T}}\boldsymbol{P}_2+(\varepsilon_1+\varepsilon_2)\boldsymbol{F}_A^{\mathrm{T}}\boldsymbol{F}_A & \boldsymbol{P}_2\boldsymbol{B} & \boldsymbol{P}_2\boldsymbol{D} & \boldsymbol{G}_2\\ * & * & -\gamma\boldsymbol{I} & \boldsymbol{0} & \boldsymbol{0}\\ * & * & * & -\gamma\boldsymbol{I} & \boldsymbol{0}\\ * & * & * & * & -\gamma\boldsymbol{I}\end{bmatrix}\\ \boldsymbol{S}_{12}=\begin{bmatrix}\boldsymbol{E}_A^{\mathrm{T}}\boldsymbol{P}_1 & \boldsymbol{0} & \boldsymbol{0} & \boldsymbol{0} & \boldsymbol{0}\\ \boldsymbol{0} & \boldsymbol{E}_A^{\mathrm{T}}\boldsymbol{P}_2 & \boldsymbol{0} & \boldsymbol{0} & \boldsymbol{0}\end{bmatrix}^{\mathrm{T}}\\ \boldsymbol{S}_{21}=\begin{bmatrix}\boldsymbol{E}_A^{\mathrm{T}}\boldsymbol{P}_1 & \boldsymbol{0} & \boldsymbol{0} & \boldsymbol{0} & \boldsymbol{0}\\ \boldsymbol{0} & \boldsymbol{E}_A^{\mathrm{T}}\boldsymbol{P}_2 & \boldsymbol{0} & \boldsymbol{0} & \boldsymbol{0}\end{bmatrix}\\ \boldsymbol{S}_{22}=\begin{bmatrix}-\varepsilon_1\boldsymbol{I} & \boldsymbol{0}\\ \boldsymbol{0} & -\varepsilon_2\boldsymbol{I}\end{bmatrix}\end{cases} \tag{A5}$$

Substituting $\boldsymbol{A}_{\mathrm{p}}$ and $\boldsymbol{B}_{\mathrm{p}}$ from (18) into (A2), $\boldsymbol{I}_{\mathrm{LMI1}}$ can be expressed as (A3). By Lemma 1, there exist scalars $\varepsilon_1$ and $\varepsilon_2$ such that (A4) holds.

Defining $\boldsymbol{S}_{11}$, $\boldsymbol{S}_{12}$, $\boldsymbol{S}_{21}$, and $\boldsymbol{S}_{22}$ as shown in (A5), $\boldsymbol{I}_{\mathrm{LMI2}}$ can be expressed as $\boldsymbol{I}_{\mathrm{LMI2}}=\boldsymbol{S}_{11}-\boldsymbol{S}_{12}\boldsymbol{S}_{22}^{-1}\boldsymbol{S}_{12}^{\mathrm{T}}$.

By the Schur complement lemma [46], since $\boldsymbol{S}_{22}<0$, $\boldsymbol{I}_{\mathrm{LMI2}}=\boldsymbol{S}_{11}-\boldsymbol{S}_{12}\boldsymbol{S}_{22}^{-1}\boldsymbol{S}_{12}^{\mathrm{T}}<0$ is equivalent to (A6).

$$\boldsymbol{S}=\begin{bmatrix}\boldsymbol{S}_{11} & \boldsymbol{S}_{12}\\ \boldsymbol{S}_{21} & \boldsymbol{S}_{22}\end{bmatrix}<0 \tag{A6}$$

Substituting $\boldsymbol{S}_{11}$, $\boldsymbol{S}_{12}$, $\boldsymbol{S}_{21}$, and $\boldsymbol{S}_{22}$ from (A5) into (A6), it can be found that (A6) is equivalent to (24). Therefore, equation (24) is a necessary and sufficient condition for $\boldsymbol{I}_{\mathrm{LMI2}}<0$. According to (A4), $\boldsymbol{I}_{\mathrm{LMI1}}\leqslant\boldsymbol{I}_{\mathrm{LMI2}}$, so (24) is the sufficient condition for $\boldsymbol{I}_{\mathrm{LMI1}}<0$. Thus, a set of $\gamma$, $\varepsilon_1$, $\varepsilon_2$, $\boldsymbol{P}_1$, $\boldsymbol{P}_2$, and $\boldsymbol{L}$ satisfying (24) can guarantee that the system in (17) is asymptotically stable and $\|\boldsymbol{T}_{\mathrm{ezd}}(\mathrm{j}\omega)\|_\infty<\gamma$.

## ACKNOWLEDGMENT

Not applicable.

## AUTHORS' CONTRIBUTIONS

Ye Tian: background research, theoretical analysis,

simulation validations, experiment validations and full-text writing. Bowen Liu: experiment validations and manuscript revision. Chushan Li: the construction of the paper framework, supervision and manuscript review & editing. Bowei chen: theoretical analysis. Bin Guo: background research and manuscript editing. Yongjun Zheng: background research and manuscript editing. Haoze Luo: supervision and manuscript review. Wuhua Li: supervision and manuscript review. Xiangning He: supervision and manuscript review. All authors read and approved the final manuscript.

## FUNDING

This work is supported by the National Key Research and Development Program of China (No. 2022YFE0138400) and Zhejiang Provincial Key R&D Program Project (No. 2023C01061).

## AVAILABILITY OF DATA AND MATERIALS

Not applicable.

## DECLARATIONS

Competing interests: The authors declare that they have no known competing financial interests or personal relationships that could have appeared to influence the work reported in this article.

## AUTHORS' INFORMATION

**Ye Tian** was born in Henan province, China. He received the B.S. degree in electrical engineering, in 2017, from the College of Electrical Engineering, Zhejiang University, Hangzhou, China, where he is currently working toward the Ph.D. degree in electrical engineering with the College of Electrical Engineering. His research interests include the condition monitoring of the power electronic device and system.

**Bowen Liu** was born in Shandong province, China. She received the B.S. degree in electrical engineering, in 2022, from the College of Electrical Engineering, Zhejiang University, Hangzhou, China, where she is currently working toward the M.S. degree in electrical engineering with the College of Electrical Engineering. Her research interests include the thermal digital twin and reliability analysis of power electronic devices.

**Chushan Li** received the B.E. and Ph.D. degrees in electrical engineering from the Department of Electrical Engineering, Zhejiang University, Hangzhou, China, in 2008 and 2014, respectively. He is currently an assistant professor with Zhejiang University–University of Illinois at Urbana Champaign Institute, Zhejiang, China. From April 2008 to September 2008, he was an internship student with the Power Application Design Center in National Semiconductor Hong Kong Company, Ltd., Hong Kong. From December 2010 to October 2011, he was a visiting scholar with FREEDM Center, North Carolina State University, Raleigh, NC, USA. From December 2013 to June 2014, he was a research assistant with Hong Kong Polytechnic University, Hong Kong. From July 2014 to July 2017, he was a postdoctoral fellow with the Department of Electrical and Computer Engineering, Ryerson University, Toronto, ON, Canada. His research interests include high-power density power converter design and transportation electrification.

**Bowei Chen** was born in Jiangxi province, China. He is working towards the B.S. degree in electrical engineering from the College of Electrical Engineering, Zhengzhou University, Zhengzhou, China. His research interest is temperature estimation of power semiconductor devices.

**Bin Guo** was born in Shandong province, China. He received the master's degree in test measurement technology and instrumentation, in 2003, from the China Institute of Metrology, Beijing, China, and currently serves as the general manager of Hangzhou Wolei Intelligent Technology Co., Ltd. His research interests include detection system design of power semiconductor device.

**Yongjun Zheng** was born in Zhejiang province, China. He received the Ph.D degree in control theory and control engineering, in 2017，from the College of Electrical Engineering, Zhejiang University, Hangzhou, China, and currently serves as an associate professor at China Jiliang University. His research interests include reliability analysis and application design of power semiconductor device.

**Haoze Luo** received the B.S. degree in electrical engineering and automation and the M.S. degree in power electronics and power drives from the Hefei University of Technology, Hefei, China, in 2008 and 2011, respectively, and the Ph.D. degree in power electronics and power drives from Zhejiang University, Hangzhou, China, in 2015. From January to April 2015, he was a visiting researcher with Newcastle University, Newcastle upon Tyne, U.K. From 2015 to 2018, he was a postdoc with the Department of Energy Technology, Aalborg University, Aalborg, Denmark. From 2018 to 2019, he was a senior R&D engineer with Dynex Power Inc., Lincoln, U.K. Since October 2019, he has been with Zhejiang University, as a research professor. He has authored or coauthored more than 100 peer-reviewed technical papers and holds more than 30 issued/pending patents. His research interests include packaging technology and reliability assessment for high-power modules. Dr. Luo was the recipient of the

outstanding reviewer for *IEEE Transactions on Power Electronics* (2021), and the "star reviewer" for *IEEE Journal of Emerging and Selected Topics in Power Electronics* (2023).

**Wuhua Li** received the B.Sc. and Ph.D. degrees in power electronics and electrical engineering from Zhejiang University, Hangzhou, China, in 2002 and 2008, respectively. From 2004 to 2005, he was a research intern, and from 2007 to 2008, a research assistant with GE Global Research Center, Shanghai, China. From 2008 to 2010, he joined the College of Electrical Engineering, Zhejiang University, as a post doctor. In 2010, he was promoted as an associate professor. Since 2013, he has been a full professor with Zhejiang University. From 2010 to 2011, he was a postdoctoral fellow with the Department of Electrical and Computer Engineering, Ryerson University, Toronto, ON, Canada. He is currently the executive deputy director of the National Specialty Laboratory for Power Electronics and the vice director of the Power Electronics Research Institute, Zhejiang University. He has authored or co-authored more than 300 peer-reviewed technical papers and holds over 50 issued/pending patents. His research interests include power devices, converter topologies, and advanced controls for high power energy conversion systems. Dr. Li was the recipient of the 2012 Delta Young Scholar from Delta Environmental & Educational Foundation, 2012 Outstanding Young Scholar from National Science Foundation of China (NSFC), 2013 Chief Youth Scientist of National 973 Program, 2014 Young Top-Notch Scholar of National Ten Thousand Talent Program, and 2019 Distinguished Young Scholar from National Science Foundation of China, due to his excellent teaching and research contributions. He was also the recipient of one National Natural Science Award and four Scientific and Technological Achievement Awards from Zhejiang Provincial Government and the State Educational Ministry of China. Since 2014, he has been the most cited Chinese researcher by Elsevier. He serves as the associated editor for *IEEE Journal of Emerging and Selected Topics in Power Electronics*, *IET Power Electronics*, *CSEE Journal of Power and Energy Systems*, *CPSS Transactions on Power Electronics and Applications*, *Proceedings of the Chinese Society for Electrical Engineering*, guest editor for *IET Renewable Power Generation* for special issue "DC and HVDC system technologies," and member of editorial board for *Journal of Modern Power System and Clean Energy*.

**Xiangning He** received the B.Sc. and M.Sc. degrees from Nanjing University of Aeronautical and Astronautical, Nanjing, China, in 1982 and 1985, respectively, and the Ph.D. degree from Zhejiang University, Hangzhou, China, in 1989, all in electrical engineering. From 1985 to 1986, he was an assistant engineer with the 608 Institute of Aeronautical Industrial General Company, Zhuzhou, China. From 1989 to 1991, he was a lecturer with Zhejiang University. In 1991, he obtained a fellowship from the Royal Society of U.K., and conducted research with the Department of Computing and Electrical Engineering, Heriot-Watt University, Edinburgh, U.K., as a post-doctoral research fellow for two years. In 1994, he joined Zhejiang University as an associate professor. Since 1996, he has been a full professor with the College of Electrical Engineering, Zhejiang University. He was the director of the Power Electronics Research Institute, the head of the Department of Applied Electronics, the vice dean of the College of Electrical Engineering, and he is currently the director of the National Specialty Laboratory for Power Electronics, Zhejiang University. His research interests include power electronics and their industrial applications. Dr. He is a fellow of the Institution of Engineering and Technology (formerly IEE), U.K. He was appointed as IEEE distinguished lecturer by the IEEE Power Electronics Society, in 2011 to 2015.

## REFERENCES

[1] S. Singh, S. Saini, and S. Gupta *et al.*, "Solar-PV inverter for the overall stability of power systems with intelligent MPPT control of DC-link capacitor voltage," *Protection and Control of Modern Power Systems*, vol. 8, no. 1, pp. 1-20, Jan. 2023

[2] H. Guo, F. Ding, and L. Ren *et al.*, "Adaptive mode switching and power management of a solid-state transformer-based active distribution network," *Power System Protection and Control*, vol. 51, no. 3, pp. 89-98, Feb. 2023. (in Chinese)

[3] G. Xu, L. Shao, and X. Xu *et al.*, "Degradation state analysis of the IGBT module based on apparent junction temperature," *Protection and Control of Modern Power Systems*, vol. 8, no. 4, pp. 1-14, Oct. 2023.

[4] Y. Yang and P. Zhang, "A novel converter-level IGBT junction temperature estimation method based on the bus voltage ringing," *IEEE Transactions on Power Electronics*, vol. 37, no. 4, pp. 4553-4563, Apr. 2022.

[5] C. H. van der Broeck, R. D. Lorenz, and R. W. De Doncker, "Monitoring 3-D temperature distributions and device losses in power electronic modules," *IEEE Transactions on Power Electronics*, vol. 34, no. 8, pp. 7983-7995, Aug. 2019.

[6] Y. Chen, Q. Wu, and Y. Zhou *et al.*, "Physics-based thermal impedance model for power module by analytic Fourier series based heat spreading angle," *Proceedings of the CSEE*, vol. 42, no. 2, pp. 715-728, Jan. 2022. (in Chinese)

[7] M. Xu, K. Ma, and Y. Qi *et al.*, "Frequency-domain thermal coupling model of multi-chip power module," *IEEE Transactions on Power Electronics*, vol. 38, no. 5, pp. 6522-6532, Jan. 2023.

[8] Y. Zhang, Z. Wang, and H. Wang *et al.*, "Artificial intelligence-aided thermal model considering cross-coupling effects," *IEEE Transactions on Power*

*Electronics*, vol. 35, no. 10, pp. 9998-10002, Oct. 2020.

[9] W. Guo, M. Ma, and H. Wang *et al*., "A thermal estimation method for IGBT module adaptable to operating conditions," *IEEE Transactions on Power Electronics*, vol. 36, no. 6, pp. 6147-6152, Jun. 2021.

[10] A. S. Bahman, K. Ma, and F. Blaabjerg, "A lumped thermal model including thermal coupling and thermal boundary conditions for high-power IGBT modules," *IEEE Transactions on Power Electronics*, vol. 33, no. 3, pp. 2518-2530, Mar. 2018.

[11] J. Li, A. Castellazzi, and M. A. Eleffendi *et al.*, "A physical RC network model for electrothermal analysis of a multichip SiC power module," *IEEE Transactions on Power Electronics*, vol. 33, no. 3, pp. 2494-2508, Mar. 2018.

[12] C. Batard, N. Ginot, and J. Antonios, "Lumped dynamic electrothermal model of IGBT module of inverters," *IEEE Transaction on Components, Packaging and Manufacturing Technology*, vol. 5, no. 3, pp. 355-364, Mar. 2015.

[13] M. Ma, W. Guo, and X. Yan *et al*., "A three-dimensional boundary-dependent compact thermal network model for IGBT modules in new energy vehicles," *IEEE Transactions on Industrial Electronics*, vol. 68, no. 6, pp. 5248-5258, Jun. 2021.

[14] C. Zhan, L. Zhu, and W. Wang *et al.*, "A large-scale identification approach for thermal parameters of multi-chip IGBT modules based on LLSO-SQP algorithm," *IEEE Journal of Emerging and Selected Topics in Power Electronics*, vol. 11, no. 3, pp. 2554-2564, Jun. 2023.

[15] Y. Lu, E. Xiang, and Y. Jin *et al.*, (2024, Jan.), "A 3-D temperature-dependent thermal model of IGBT modules for electric vehicle application considering various boundary conditions," *IEEE Journal of Emerging and Selected Topics in Power Electronics*, [Online], Avaliable: https://ieeexplore.ieee.org/document/10404062

[16] K. Heng, X. Yang, and X. Wu *et al.*, "A 3-D thermal network model for monitoring of IGBT modules," *IEEE Transactions on Electron Devices*, vol. 70, no. 2, pp. 653-661, Feb. 2023.

[17] K. Heng, X. Yang, and X. Wu *et al.*, "A temperature-dependent physical thermal network model including thermal boundary conditions for SiC MOSFET module," *IEEE Transactions on Electron Devices*, vol. 69, no. 8, pp. 4444-4452, Aug. 2022.

[18] X. Yang, K. Heng, and X. Dai *et al.*, "A temperature-dependent Cauer model simulation of IGBT module with analytical thermal impedance characterization," *IEEE Journal of Emerging and Selected Topics in Power Electronics*, vol. 10, no. 3, pp. 3055-3065, Jun. 2022.

[19] X. Yang, S. Xu, and K. Heng *et al.*, "Distributed thermal modeling for power devices and modules with equivalent heat flow path extraction," *IEEE Journal of Emerging and Selected Topics in Power Electronics*, vol. 11, no. 6, pp. 5863-5876, Dec. 2023.

[20] T. Han, Y. Luo, and B. Liu *et al.*, "A reduced-order decoupling method applied to efficient junction temperature simulation model in multi-chip devices," *IEEE Journal of Emerging and Selected Topics in Power Electronics*, vol. 11, no. 5, pp. 5405-5416, Oct. 2023

[21] W. Guo, M. Ma, and H. Wang *et al.*, "Real-time average junction temperature estimation for multi-chip IGBT modules with low computational cost," *IEEE Transactions on Industrial Electronics*, vol. 70, no. 4, pp. 4175-4185, Apr. 2023.

[22] Y. Shi, J. Liu, and Y. Ai *et al.*, "Dynamic IGBT three-dimensional thermal network model considering base solder degradation and thermal coupling between IGBT chips," *IEEE Transactions on Transportation Electrification*, vol. 9, no. 2, pp. 2994-3011, Jun. 2023.

[23] Y. Fan, H. Cui, and Z. Luo *et al.*, "Base solder voids identification of IGBT modules using case temperature," *Microelectronics Reliability*, vol. 115, Dec. 2020.

[24] Z. Hu, M. Du, and K. Wei *et al.*, "An adaptive thermal equivalent circuit model for estimating the junction temperature of IGBTs," *IEEE Journal of Emerging and Selected Topics in Power Electronics*, vol. 7, no. 1, pp. 392-403, Mar. 2019.

[25] Z. Wang, B. Tian, and W. Qiao *et al.*, "Real-time aging monitoring for IGBT modules using case temperature," *IEEE Transactions on Industrial Electronics*, vol. 63, no. 2, pp. 1168-1178, Feb. 2016.

[26] M. Akbari, M. Tavakoli Bina, and A. S. Bahman *et al.*, "An extended multilayer thermal model for multichip IGBT modules considering thermal aging," *IEEE Access*, vol. 9, pp. 84217-84230, May 2021.

[27] H. Fu, J. Chen, and A. S. Bahman *et al.*, "An online identification method of thermal dissipation state for a forced air-cooled system of power converters," *IEEE Journal of Emerging and Selected Topics in Power Electronics*, vol. 10, no. 6, pp. 7677-7690, Dec. 2022.

[28] H. Fu, J. Chen, and H. Wang *et al.*, "3-D-lumped thermal network models for the reliability analysis of fan-cooled plate-fin heatsink," *IEEE Journal of Emerging and Selected Topics in Power Electronics*, vol. 11, no. 3, pp. 3480-3491, Jun. 2023.

[29] J. Cai, L. Zhou, and P. Sun *et al.*, "Effect of TIM deterioration on monitoring of IGBT module thermal resistance and its compensation strategy," *IEEE Transactions on Components, Packaging, and Manufacturing Technology*, vol. 12, no. 5, pp. 789-797, May 2022.

[30] X. Yan, M. Ma, and W. Guo *et al.*, " A fast and accurate junction temperature estimation method of IGBT modules for PMSM drives considering multiple working conditions," in *2020 IEEE 9th International Power Electronics and Motion Control Conference*, Nanjing, China, Nov. 2020, pp. 940-944.

[31] P. Liu, H. Li, and Y. Miao *et al.*, "Online junction temperature extraction for SiC module based on built-in temperature sensor," *Transactions of China Electrotechnical Society*, vol. 36, no. 12, pp. 2522-2534, Jun. 2021.

[32] J. Zhang, X. Du, and Y. Wu *et al.*, "Thermal parameter monitoring of IGBT module using case temperature," *IEEE Transactions on Power Electronics*, vol. 34, no. 8, pp. 7942-7956, Aug. 2019.

[33] J. Kuprat, K. Debbadi, and J. Schaumburg *et al.*, "Thermal digital twin of power electronics modules for online thermal parameter identification," *IEEE Journal of Emerging and Selected Topics in Power Electronics*, vol. 12, no. 1, pp. 1020-1029, Feb. 2024.

[34] H. Li, B. Zhou, and R. Yao *et al.*, "A thermal twin

modeling method of press pack IGBT based on power loss," *IEEE Transactions on Electron Devices*, vol. 69, no. 12, pp. 6922-6928, Dec. 2022.

[35] A. Arya, A. Shankar, and A. Verma *et al.*, "Multiple points measurement-based junction temperature estimation of IGBT module," *IEEE Journal of Emerging and Selected Topics in Power Electronics*, vol. 11, no. 3, pp. 3457-3467, Jun. 2023.

[36] X. Zhang, W. Mu, and C. Lü *et al.*, "A thermal network model for monitoring IGBT chip solder degradation based on feedback PI control," *Microelectronics Reliability*, vol. 138, Nov. 2022.

[37] S. Kalker, D. Meier, and C. H. van der Broeck *et al.*, "Self-calibrating loss models for real-time monitoring of power modules based on artificial neural networks," in *Proceedings of 2022 IEEE Energy Conversion Congress and Exposition (ECCE)*, Detroit, USA, Sept. 2022, pp. 1-8.

[38] X. Wang, A. Castellazzi, and P. Zanchetta, "Observer-based temperature control for reduced thermal cycling in power electronic cooling," *Applied Thermal Engineering*, vol. 64, no. 1-2, pp. 10-18, Jun. 2014.

[39] X. Dong, A. Griffo, and D. Hewitt *et al.*, "Reduced-order thermal observer for power modules temperature estimation," *IEEE Transactions on Industrial Electronics*, vol. 67, no. 12, pp. 10085-10094, Dec. 2020.

[40] M. A. Eleffendi and C. M. Johnson, "Application of Kalman filter to estimate junction temperature in IGBT power modules," *IEEE Transactions on Power Electronics*, vol. 31, no. 2, pp. 1576-1587, Feb. 2016.

[41] A. Soldati, N. Delmonte, and P. Cova *et al.*, "Device-sensor assembly FEA modeling to support Kalman-filter-based junction temperature monitoring," *IEEE Journal of Emerging and Selected Topics in Power Electronics*, vol. 7, no. 3, pp. 1736-1747, Sept. 2019.

[42] X. Xiao, X. Ge, and Q. Ke *et al.*, "An adaptive temperature observer for electrothermal analysis of IGBT based on temperature characteristics," *IEEE Journal of Emerging and Selected Topics in Power Electronics*, vol. 11, no. 2, pp. 2246-2258, Apr. 2023.

[43] Y. Tian, K. Bu, and B. Liu *et al.*, "3D thermal resistance model for real-time temperature monitoring of multi-chip IGBT modules," in *Proceedings of 2023 IEEE 2nd International Power Electronics and Application Symposium (PEAS)*, Guangzhou, China, Nov. 2023, pp. 293-298.

[44] C. Entzminger, W. Qiao, and L. Qu *et al.*, "Automated extraction of low-order thermal model with controllable error bounds for SiC MOSFET power modules," *IEEE Transactions on Power Electronics*, vol. 39, no. 1, pp. 538-551, Jan. 2024.

[45] Z. Wang, W. Qiao, and L. Qu, "A real-time adaptive IGBT thermal model based on an effective heat propagation path concept," *IEEE Journal of Emerging and Selected Topics in Power Electronics*, vol. 9, no. 4, pp. 3936-3946, Aug. 2021.

[46] L. Wu, "Research on model-based robust fault detection and estimation methods for uncertain systems," Ph.D. dissertation, the Department of Control Science and Engineering, Harbin Institute of Technology, Harbin, China, 2013.